


2012-01-01

Microscopic and Spectroscopic Analysis of WO₃ and Ti-doped WO₃ Thin Films

Young Taek Yun

University of Texas at El Paso, yyun@miners.utep.edu

Follow this and additional works at: https://digitalcommons.utep.edu/open_etd

 Part of the [Analytical Chemistry Commons](#), [Nanoscience and Nanotechnology Commons](#), and the [Oil, Gas, and Energy Commons](#)

Recommended Citation

Yun, Young Taek, "Microscopic and Spectroscopic Analysis of WO₃ and Ti-doped WO₃ Thin Films" (2012). *Open Access Theses & Dissertations*. 2416.

https://digitalcommons.utep.edu/open_etd/2416

This is brought to you for free and open access by DigitalCommons@UTEP. It has been accepted for inclusion in Open Access Theses & Dissertations by an authorized administrator of DigitalCommons@UTEP. For more information, please contact lweber@utep.edu.

MICROSCOPIC AND SPECTROSCOPIC ANALYSIS OF WO₃ AND TI-DOPED WO₃ THIN
FILMS

YOUNG TAEK YUN

Material Science and Engineering

APPROVED:

Felicia F. Manciu, Ph.D., Chair

Lawrence Murr, Ph.D.

Russell Chianelli, Ph.D.

Roy Arrowood, PhD.

William Durrer, PhD.

Benjamin C. Flores, Ph.D.
Interim Dean of the Graduate School

Copyright ©

by

Young Take Yun

2012

Dedication

My sincere dissertation dedication goes to my one and only wife and daughter, and to my mother and family, who always hope for the best for me

MICROSCOPIC AND SPECTROSCOPIC ANALYSIS OF WO₃ AND TI-DOPED WO₃ THIN
FILMS

by

YOUNG TAEK YUN MS

DISSERTATION

Presented to the Faculty of the Graduate School of
The University of Texas at El Paso
in Partial Fulfillment
of the Requirements
for the Degree of

DOCTOR OF PHILOSOPHY

Material Science and Engineering
THE UNIVERSITY OF TEXAS AT EL PASO
May 2012

Acknowledgements

My Advisor and the great committee members have encouraged and enriched my PhD education experience at the University of Texas at El Paso. First and foremost, I am indebted to my advisor, Felicia Manciu. Her dedication and consistent encouragement always helped me to strive for higher achievement in life. Knowing her and following in her footsteps have been a life changing experience. My sincere respect also goes to the man of integrity, the great-to-be-with Dr Murr. After taking 5 of his classes, I was looking for more and his lectures were more than mere acquisition of knowledge; they contained life lessons and his passion. The connection between science and real life has been demonstrated by Dr. Chianelli who has invited experts from everywhere in industry to inspire his students with an abundance of science applications; I personally appreciate him for teaching real applications of science and the importance of inter-disciplinary study. Dr. Arrowood opened the world of material science and helped me to understand how important his field is and in the end, succeeded in pulling me into his world. Last but not the least; Dr Durrer is the scientist and the mentor in my life. The knowledge and skills that he presented to me have been treasured and I have realized that they are the heritage that I need to pass on.

My sincere gratitude also goes to the UTEP staff. The great faculty members in the Physics department and their mentorships helped me to teach physical science classes and boosted my passion for teaching. Terry Weber, with her most efficient and clear direction, helped me to work in the physics department. The administrative help and great conversations that I had with Liz Rodriguez are appreciated. Not to mention Dr Incera for her exceptional leadership; her positive karma is defining the female power in the science department next to Dr Morrobel-Sosa.

I wouldn't even dream of standing where I am now if my family's support weren't there in the first place with their continuous trust and love. My wife and mother of our daughter endowed me with consistent support and love through the course of this journey. The sacrifices of my wife and the simple smile of my daughter were the energizers pushing me forward and keeping me going. At this time, I just wanted to thank all of you who have been around me and I know this work is not done by me but humbly admit "It was team work after all".

Abstract

Tungsten oxide (WO_3) has been a subject of high interest for its unique properties, and recently for its importance in different types of industrial applications which range from non-emissive displays, optical, microelectronic, catalytic/photocatalytic, humidity, temperature, gas, and biosensor devices. In this study, WO_3 and Ti doped thin films were prepared using radio frequency magnetron reactive sputtering at different substrate temperatures ranging from room temperature to 500 °C in increments of 100 °C. After forming a hypothesis based on knowledge of established WO_3 properties, we attempt in this work to investigate how the doping influences the roughness and the mean grain size of the nanoparticles on the surface layer of the thin films, their structure, and crystallinity. Therefore we pursued analysis by Atomic Force Microscopy (AFM), X-ray diffraction (XRD), and Raman spectroscopy, using a comparative approach. The outcomes of these analyses demonstrate that higher temperatures are necessary for growing crystalline material if doping is used. Also, smaller nanoparticles are obtained when a small amount of dopant, e.g. 5% Ti, is incorporated. Both XRD and Raman measurements indicate morphology changes of the doped material. Finally, annealing of the amorphous doped samples at temperatures of 600 °C and 900 °C did not contribute significantly to material properties improvement.

Table of Contents

Acknowledgements.....	v
Abstract.....	vi
Table of Contents.....	vii
List of Tables	ix
List of Figures.....	x
Chapter 1: Introduction.....	1
1.1 INTRODUCTORY REMARKS	1
1.2 BACKGROUND AND RESEARCH MOTIVATION FOR USING METAL OXIDES...2	
1.3 STRUCTURAL AND SPECTROSCOPIC PROPERTIES OF WO ₃	8
Chapter 2: Experimental Details.....	18
2.1 INTRODUCTORY REMARKS	18
2.2 ATOMIC FORCE MICROSCOPY (AFM)	19
2.2.1 Principles of AFM.....	20
2.2.2 AFM Modes.....	21
2.2.3 AFM experimental set-up	23
2.3 X-RAY DIFFRACTION (XRD).....	24
2.3.1 X-rays and X-ray tube	25
2.3.2 Bragg's Law.....	26
2.3.3 Lattices and crystal structures.....	27
2.3.4 XRD experimental set-up	30
2.4 RAMAN SPECTROSCOPY	30
2.4.1 Classical approach	32
2.4.2 Quantum approach.....	33
2.5 SAMPLE PREPARATION.....	35
Chapter 3: Results and Discussion	37
3.1 INTRODUCTORY REMARKS	37
3.2 AFM RESULTS FOR WO ₃ THIN FILMS	37
3.3 AFM RESULTS FOR Ti(5%) DOPED WO ₃ THIN FILMS	45
3.4 X-RAY DIFFRACTION RESULTS FOR WO ₃ AND Ti(5%) DOPED WO ₃ THIN FILMS.....	52

3.5	COMPARATIVE SPECTROSCOPIC RAMAN RESULTS FOR WO ₃ , Ti(5%) DOPED WO ₃ , AND Ti(20%) DOPED WO ₃ THIN FILMS	56
3.6	FTIR ABSORPTION RESULTS FOR Ti(20%) DOPED WO ₃ THIN FILMS	61
3.7	RAMAN AND IFRARED ABSORPTION RESULTS FOR Ti(5%) DOPED WO ₃ THIN FILMS ANEALD AT 600 °C AND 900 °C.....	62
Chapter 4: Conclusion and future work.....		65
4.1	CONCLUSION.....	65
4.2	FUTURE WORK.....	67
References.....		68
Vita	74

List of Tables

Table 1.1: Atomic coordinates in fractions of edges of unit cell with lattice parameters of $a = 7.30 \text{ \AA}$, $b = 7.53 \text{ \AA}$, and $c = 7.68 \text{ \AA}$, with $\beta = 90^\circ 54'$ for monoclinic phase of WO_3 [42]	9
Table 1.2: Atomic coordinates in fractions of the unit cell edges with lattice parameters of.....	10
$a = 7.341 \text{ \AA}$, $b = 7.570 \text{ \AA}$, and $c = 7.754 \text{ \AA}$ for orthorhombic phase of WO_3 [43]	10
Table 1.3: Atomic coordinates in fractions of edges of unit cell for tetragonal phase of WO_3 [44]	11
Table 1.4: Raman vibrational frequencies associated with monoclinic and orthorhombic structures of WO_3 . [45-47]	12
Table 2.1: Comparison of resolution and capability of AFM with SEM and TEM. [52]	19
Table 2.2: The Seven Crystal Systems.....	28
Table 4.1: Literature reported WO_3 structural phases as function of temperature. [68]	58

List of Figures

Figure 1.1: Schematic diagram of band representation of MOX (in this case an n-type crystalline semiconductor). Oxygen vacancies are responsible for “-“ charges in the conduction band EC and “+” in the energy gap. The arrows show a schematic of how the reactive gases interact with the material. [Adapted after 17].....	4
Figure 1.2: Unit cell representations for WO ₃ orthorhombic and monoclinic morphologies.	9
Figure 2.1: Illustration of AFM basic components and their interactions and feedback system.[53]	21
Figure 2.2: Image of <i>WITec alpha 300 RA</i> AFM module.....	24
Figure 2.3 : Scheme of X-ray tube’s major components and of X-ray production.	26
Figure 2.4: Bragg’s law and its parameters.	27
Figure 2.5: Schematic representation of the 14 Bravais lattices.[56]	29
Figure 2.6: Bruker D8 Advance X-ray diffraction system.	30
Figure 2.7: Two types of Quantum Raman scattering – Stokes and Anti-Stokes [60,61].....	33
Figure 2.8: <i>alpha 300 WITec</i> confocal Raman system.....	35
Figure 3.1: (a) AFM image and (b) roughness profile of WO ₃ grown at room temperature.	38
Figure 3.2: (a) AFM image and (b) roughness profile of WO ₃ grown at a substrate temperature of 100 °C.....	39
Figure 3.3: (a) AFM image and (b) roughness profile of WO ₃ grown at a substrate temperature of 300 °C.....	41
Figure 3.4: (a) AFM image and (b) roughness profile of WO ₃ grown at a substrate temperature of 400 °C.....	42
Figure 3.5: (a) AFM image and (b) roughness profile of WO ₃ grown at a substrate temperature of 500 °C.....	43
Figure 3.6: (a) Grain size and (b) surface roughness versus temperature for WO ₃ films.....	44
Figure 3.7: (a) AFM image of Ti (5%) doped WO ₃ grown at a substrate	46

temperature of 100 °C.....	46
Figure 3.8: (a) AFM image of Ti (5%) doped WO ₃ grown at a substrate	47
temperature of 200 °C.....	47
Figure 3.9: (a) AFM image of Ti (5%) doped WO ₃ grown at a substrate	48
temperature of 300 °C.....	48
Figure 3.10: (a) AFM image of Ti (5%) doped WO ₃ grown at a substrate	49
temperature of 400 °C.....	49
Figure 3.11: (a) AFM image of Ti (5%) doped WO ₃ grown at a substrate	50
temperature of 500 °C.....	50
Figure 3.12: (a) Grain size and (b) surface roughness vs. temperature for Ti(5%) doped WO ₃ films.	51
Figure 3.13: X-ray diffraction patterns of WO ₃ films as a function of temperature.....	52
Figure 3.14: X-ray diffraction patterns of Ti(5%) doped WO ₃ films as a function of temperature.	54
Figure 3.15: Comparison of the diffraction peaks around 23° 2θ angle of WO ₃ and.....	55
Ti(5%) doped WO ₃ films grown at a substrate temperature of 500 °C.	55
Figure 3.17: Raman spectra of Ti(20%)-doped WO ₃ samples grown at	59
Si substrate temperatures ranging between RT and 500 °C.....	59
Figure 3.18: Raman spectra of pure, Ti(5%)-, and Ti (20%)-doped WO ₃	60
samples grown at a substrate temperature of 500 °C.....	60
Figure 3.19: Infrared absorption spectra of Ti(20%)-doped WO ₃ samples grown at.....	61
Si substrate temperatures ranging between RT and 500 °C.....	61
Figure 3.20: Raman spectra of Ti(20%)-doped WO ₃ samples annealed at 600 °C and 900 °C.	62
For comparison, the spectrum of pure WO ₃ grown at a substrate temperature	62
of 500 °C is presented, too.	62
Figure 3.21: Infrared absorption spectra of Ti(20%)-doped WO ₃ samples annealed	63
at 600 °C and 900 °C.....	63

Chapter 1: Introduction

1.1 INTRODUCTORY REMARKS

The goal of this research is to provide, from a comparative perspective, detailed microscopic and spectroscopic characterization of tungsten oxide (WO_3) and of Ti-doped WO_3 using atomic force microscopy (AFM), X-ray diffraction (XRD), and Raman spectroscopy. Since this research was supported by a grant from Department of Energy, the work presented here is also linked to the demand for advancements in the performance of materials used in sensors for detection of poisoning gases in the coal-gasification process.

With increased demands for and interests in clean energy and abundant reservoirs of coal in the United States, there have been focused efforts to develop the Integrated Gasification Combined Cycle (IGCC), which can offer higher efficiency and a lower pollution emission cycle, and, eventually, enhance fossil fuel energy production. Unwanted byproducts of this cycle need to be vigilantly monitored and controlled throughout the entire process. The need for this monitoring of poisonous gases gives rise to a call for development of sensor materials with high-sensitivity and selectivity, as well as with real time detection capability.[1-3]

Thus, high quality materials that will be resistant at high temperatures, a condition that is characteristic of coal-gasification processes, are required for achieving this objective. However, before any material gas testing or its use in sensor packaging can be done, tasks that are beyond the scope of this work, the effect of processing conditions on the growth and microstructural evolution of undoped and Ti-doped WO_3 thin-films and their properties at the nano-scale needs to be systematically studied in order to develop stable microstructures and reliable materials.

Material Characterization can be defined as the use of external techniques to explore the internal structure and properties of a material [4]. *Characterization* can take the form of actual materials testing or analysis. It is hard to pinpoint in time and place the origin of *Material Characterization*. Historically, Lawrence Bragg and Sir Chandrasekhara Venkata Raman have been distinguished as two major players to develop the *Material Characterization* technical field. The invention of X-ray crystallography in the early 1900s by William Lawrence Bragg enabled innovation, not to mention that Bragg's law is still fundamental for today's material scientists. Also, Raman scattering or the Raman effect, which is the inelastic scattering of photons, was discovered by Sir C. V. Raman in 1928. Later, in 1980, the first system to perform atomic force microscopy (*e.g.* scanning tunneling microscope) was developed by Gerd Binnig and Heinrich Rohrer at IBM Research in Zurich. It is also interesting to note that the progress in different research areas has often been fueled by the demands of industry, well ahead of purely academic curiosity.

The subsequent sections will contain an overview of previous studies that have been done on metal oxides, along with the scientific trend in developing and enhancing their characteristics as sensor materials. Being the main purpose of this research, an emphasis will be put on pure and doped WO_3 materials; especially on their microscopic, structural, and spectroscopic properties.

1.2 BACKGROUND AND RESEARCH MOTIVATION FOR USING METAL OXIDES

Ever since WO_3 was synthesized and patented by Robert Oxland in 1841, tremendous interest and development of applications have occupied scientists and engineers around the world. Initially tungsten oxide (WO_3) received much attention because of its electrochromic and photochromic properties; later on, it has stimulated interest as a material with good prospects for use in gas sensing. Due to the controllable changeability of its optical properties, which is also reversible, the following innovative applications have been out in the market: electrochromic camera displays, anti-dazzling rear

view mirrors for automobiles, smart windows and glass facades that can regulate visible light and solar energy to improve indoor comfort.[2,5-7] The mechanism behind developing these types of sensors was based on controlling the opacity of the transparent thin film using variation of their thicknesses or by controlling their reversible coloration via electrochemical processes.

The research and development group of Huang *et al.* [2] recently explored the potential of WO₃ nanowires as sensing elements for UV light photodetection and as a result, high-sensitivity nanoscale UV detectors and optoelectronic switching devices came to light. By using Na₂SO₄ as a structuring agent, a simple hydrothermal coating was used to apply WO₃ to a nanowire. An interesting fact was found along with the nanowire research: while thin amorphous wire was exposed to WO₃, both optical absorptivity and electrical conductivity increased in addition to the expected change of the color.[7] Furthermore, potentially limitless applications also include non-emissive displays, optical and microelectronic devices, catalytic/photocatalytic processing, humidity sensors, temperature sensors, biosensors, and photonic crystals.[8-11]

Metal oxide (MOX) sensors have been also utilized for several decades for detection of combustible and toxic gases because of low cost, relative simplicity of implementation, and good reliability. It is not hard to see that oxygen is the common element in these compounds and plays a major roll in the detection mechanisms at sensor surfaces. The mechanism for gas detection by MOX materials is based, in large part, on reactions that occur at the sensor surface, resulting in a change in the concentration of adsorbed oxygen. Oxygen ions adsorb onto the material's surface, removing electrons from the bulk and creating a potential barrier that limits electron movement and conductivity. When the reactive gases are combined with this oxygen, the height of the barrier is reduced, increasing conductivity. This change in conductivity is directly related to the amount of a specific gas present in the environment, enabling a quantitative determination of gas presence and concentration.

Gopel and Schierbaum [12] defined a chemical sensor as device which converts a chemical state into an electrical signal, where the concept of chemical state is considered to take the form of different concentrations or partial pressures of molecules or ions in a gas, liquid, or solid phase.

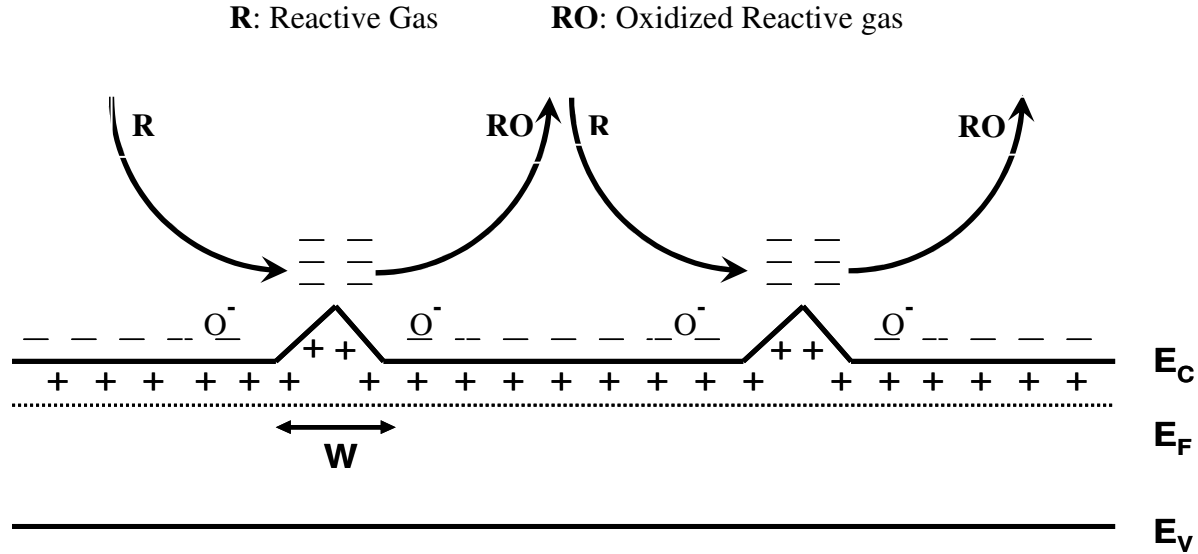


Figure 1.1: Schematic diagram of band representation of MOX (in this case an n-type crystalline semiconductor). Oxygen vacancies are responsible for “-“ charges in the conduction band E_C and “+” in the energy gap. The arrows show a schematic of how the reactive gases interact with the material. [Adapted after 17]

In this context, chemical sensors are interfaces between chemistry and electronics that contain, mainly, two domains: the chemical interface layer and the physical transducer, the former shown in **Figure 1.1**. [12-17] Since the interface layer is the platform where the chemical/physical changes are produced due to interactions between the measured substance and the surface layer, it needs [12-17]:

- To keep the minimum interactive distance with the substance to be measured.
- To be highly sensitive to the exposed substance.
- To be physically small and more economical than other comparable systems.
- To be able to detect more than a single chemical or physical property.
- To maintain its mechanical structure for long hours of operation.

- To yield a linear or proportional relationship to chemical changes so that the physical transducer can generate a related electrical signal in a single manner.

WO₃ is also categorized as an n type semiconductor and a common characteristic of this type of material is the stoichiometric excess of the metal, and one generally accepted theory for explaining its behavior is the presence of oxygen vacancies. It is also worthy to note, because most of the interface is the surface, higher conductivity has been reported at the surface than in the bulk material. A theoretical approach was developed and is known as the Schottky barrier at interparticle contacts, which describes how the surface oxygen, with negative two oxidation number attracts the surrounding electrons.[18-21] Because the electrons originate from ionized donors via the conduction band, the charge carrier density at the interface is reduced and a potential barrier to charge transport appears, inhibiting the adsorption of further oxygen. Near the grain surface, then, the depletion layer with its potential barrier can become a high resistance region, but one which will be sensitive to the coverage of adsorbed oxygen ions on the surface. The temperature variance of the oxygen vacancies was experimentally verified: O²⁻ is dominant at 200 °C or less; between 200 °C and 500 °C, there is a higher occurrence of O⁻, and at 500 °C or higher, lattice oxygen is balanced with the surrounding atmosphere.[18-21] Thus, although indirectly, the sample growth temperature could be related not only to a change in the structural phase of the material, but also to the amount of oxygen vacancies.

In view of the fact that oxide materials have the characteristics stated above, some of them that have been researched and used for detecting various gases such as O₃, O₂, NO₂, NO, NH₃, N₂, H₂, H₂S, and ethanol are: [22-30]

Semiconducting oxides: WO₃, TiO₂, SnO₂, ZnO, In₂O₃, and Fe₂O₃

Catalytic Oxides: VO, MoO₃, CuO, NiO

Before discussing the sensitivity of WO₃, the advantages and disadvantages of few of the above solid state materials are worth mentioning. Let us start with ZnO, since it is one of the earliest materials

that were developed for gas detection and the most widely applied oxide gas sensing material.[31-33] For example, only about 25% sensitivity to 30 ppm of NH_3 was found for this material at room temperature[31]. Chen *et al.* found the gas sensitivity of ZnO nanoflakes to 0.5 ppm NO_2 increased with increasing sample calcination temperature. They reported that the sample annealed at 500 $^{\circ}\text{C}$ exhibited the maximum sensitivity for an operating temperature ranging from 129 $^{\circ}\text{C}$ to 230 $^{\circ}\text{C}$. [32] Also, Zhang *et al.* reported an augmented sensitivity at room temperature for H_2S for ZnO dendritic samples that were synthesized at a temperature of 930 $^{\circ}\text{C}$. [33] They explained this behavior based on the modulation of the energy barrier at contacts between ZnO nanorods. Another material is SnO_2 . Barsan and Weimar in their study demonstrated that SnO_2 sensor material completely eliminates the influence of water for CO concentrations in the range of 50-500 ppm and temperatures between 250 to 400 $^{\circ}\text{C}$. [34] It has also been reported that In_2O_3 has a maximum sensitivity to ethanol vapor concentrations up to 80 ppm for a temperature of 350 $^{\circ}\text{C}$. [35] Even in this study, not only structural changes of In_2O_3 films such as surface electromigration of In atoms had been observed when material was exposed to the gas, but also degradation effects caused by the simultaneous influence on In_2O_3 films of elevated temperatures and other environmental conditions. [35] Enhancement in the quality of this material have been reported when quasi-one dimensional (1D) In_2O_3 wires were used. [30]. Furthermore, Ferroni *et al.* demonstrate that nanosize structured TiO_2 can be effectively used as a gas sensor material for engine exhaust pipes, since it has the capability of detecting 20 ppm NO_2 at the typical environmental temperatures. [36]

WO_3 in either case is categorized both as a metal oxide (MOX) and as a semiconducting oxide, thus retaining all the aforementioned advantages of MOX. As gas sensor material, it is known that WO_3 has been considered for detecting O_3 , NO_x , NH_3 , H_2 , and H_2S . [22-30] It has also been demonstrated to be less sensitive to carbon monoxide and hydrocarbons than it is to the previously mentioned gases and to volatile organic compounds (VOC) that can cause serious health problems. [22]

If H_2S is the targeted gas for the sensor material, perovskite type metal oxides such as WO_3 are the materials of choice for sensing. H_2S is a very toxic gas known to be produced in active volcanic fumaroles prior to eruption. It is also identified as a primary chemical component in the atmosphere of Venus and as a pollutant generated during numerous chemical processes, including combustion. The threshold limited value (TLV) is 10 ppm and when the concentration is higher than 250 ppm, it is dangerous to the human body and may cause death.[37]

WO_3 based semiconducting metal oxide sensors have received great attention for H_2S detection. For example, WO_3 films made by a RF sputtering deposition method, when employed in gas sensing, showed that as-deposited films were sub-stoichiometric with various O/W ratios under 2.9.[27] The interaction with H_2S was studied at 475 K, where the sensitivity of the film to the H_2S gas is highest.[28] The gas sensor's change in conductivity is most likely caused by the formation of a steady-state concentration of surface oxygen vacancies when the sensor is exposed to a given partial pressure of H_2S in air.[38,39] Moreover, the H_2S response properties of the WO_3 thin film sensors were studied both in dry and wet synthetic air with different levels of humidity.[19,30] It has been noted that sputtered WO_3 thin-film sensors give a large variation between the H_2S response properties of different sensors in the same sensor array where some sensors were found to be sensitive to H_2S in the ppb range without gold doping, but give a slight increase in the conductance of the sensors in humid environments, which interfere to some extent with the H_2S sensing.[5,29,38] Also, thin vs. thick WO_3 films as sensing layers were also studied with regard to the stability and functionality of the sensors.[23-25] It has been known that the resistivity of thin films decrease when reactive gases interact with the surface, while thick films show an increment in resistance value under the same conditions.

Thus, metal oxide sensing properties as well as their other characteristics depend highly on crystallinity, grain size, nanoporosity, and stoichiometry. Since an important question to consider is the degree to which doping can affect the porosity of the WO_3 film structure and/or its chemistry, which can

have an influence on the effective surface area and ultimately can determine the number of surface active sites for oxygen adsorption, an analysis of these samples at a molecular level could bring additional valuable insights. However, information about the structural and spectroscopic properties of pure WO_3 is essential before advancing to analysis of other tungsten oxide types of engineered materials (e.g. morphological modification induced by doping). Thus, below we present these known properties for pure WO_3 .

1.3 STRUCTURAL AND SPECTROSCOPIC PROPERTIES OF WO_3

Ever since tungsten was discovered in the 18th century by Peter Woulfe, the element has been of extensive interest to many scientists all over the world. It is known to have the highest melting point ($T_m = 3422^\circ\text{C}$) of all the non-alloyed metals and the second highest of all the elements after carbon ($T_m = 3550^\circ\text{C}$). Also remarkable is its high density of 19.3 times that of water.[40] However, pure tungsten is brittle even though it is very hard, so it is very hard to work with.[41] The unalloyed elemental form is used in most applications. Tungsten's many alloys have numerous applications, most notably in incandescent light bulb filaments, X-ray tubes (as both the filament and target), and superalloys. Tungsten's hardness and high density give it military applications in penetrating projectiles. From the periodic table, two oxidation numbers assigned to tungsten are +6 and +4. With these states and in combination with the most abundant material on earth, it exists in the following three common forms of compounds; W_2O_3 , WO_2 , and WO_3 .

Among them, WO_3 with a structure similar to that of rhenium oxide ReO_3 but a symmetry lowered by two distortions (the tilting of WO_6 octahedra and the displacement of W from the center of its octahedron) has been the subject of highest interest because of its unique properties, as mentioned before. Its melting temperature is 1473°C and its density is 7.16 g/cm^3 and the crystal structure is known to be monoclinic at room temperature.[42,43] However, its structure changes with the

temperature and so far it is found to have 11 different phases and four different crystal structures – triclinic from 25-30 °C, monoclinic from 30-330 °C, orthorhombic from 330-740 °C, and tetragonal from 740-1437 °C.[42,43] Two different morphologies of WO₃, the monoclinic (space group P2₁/n) and the orthorhombic (space group P_{mnb}) ones, are presented in Figure 1.2. They were obtained using Diamond® 2.1 software. The corresponding atomic coordinates are listed in Tables 1.1 and 1.2.

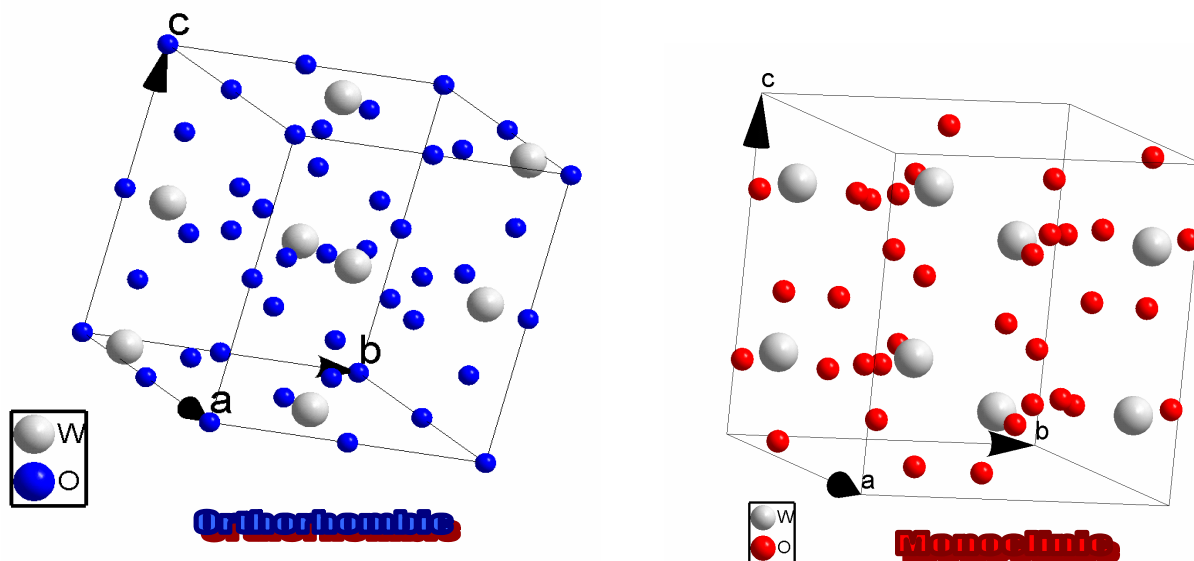


Figure 1.2: Unit cell representations for WO₃ orthorhombic and monoclinic morphologies.

Table 1.1: Atomic coordinates in fractions of edges of unit cell with lattice parameters of $a = 7.30 \text{ \AA}$, $b = 7.53 \text{ \AA}$, and $c = 7.68 \text{ \AA}$, with $\beta = 90^\circ 54'$ for monoclinic phase of WO₃ [42]

Coordinates /Atom	X	Y	Z
W ₁	0.252	0.026	0.0285
W ₂	0.247	0.033	0.0781

O_{x1}	0	0.025	0.22
O_{x2}	0	0.475	0.22
O_{y1}	0.29	0.29	0.265
O_{y2}	0.21	0.29	0.735
O_{z1}	0.28	0.040	0.030
O_{z2}	0.28	0.49	0.030

Table 1.2: Atomic coordinates in fractions of the unit cell edges with lattice parameters of

$a = 7.341 \text{ \AA}$, $b = 7.570 \text{ \AA}$, and $c = 7.754 \text{ \AA}$ for orthorhombic phase of WO_3 [43]

Coordinates /Atom	X	Y	Z
W₁	0.25	0.029	0.031
W₂	0.25	0.030	0.0532
O₁	0	0	0
O_{1'}	0.5	0	0
O₂	0	0	0.5
O_{2'}	0.5	0.5	0
O₃	0.25	0.269	0.027
O₄	0.25	0.278	0.471
O₅	0.25	0.004	0.262
O₅	0.25	0.015	0.776

According to Locherer and Salje [44], the tetragonal phase of WO_3 has the lattice parameters $a = 5.25 \text{ \AA}$ and $c = 3.88 \text{ \AA}$. The space group was found to be $P4/nmm$, and the atomic parameters, in fractions of the cell edges, are given in Table 1.3.

Table 1.3: Atomic coordinates in fractions of edges of unit cell for tetragonal phase of WO_3 [44]

Coordinates /Atom	X	Y	Z
W₁	0.250	0.250	0.0729
W₂	0.250	0.250	0.0664
O_{x1}	0.250	0.250	0.478
O_{x2}	0.250	0.250	0.494
O_{y1}	0	0	0
O_{y2}	0	0	0

Raman vibrational modes for different structural phases of WO_3 such as monoclinic, and orthorhombic have been also been reported in the literature, theoretically as well as experimentally. These findings are summarized in Table 1.4. It can be observed from this table that the vibrations associated with different phases of WO_3 , for example those of monoclinic and orthorhombic morphologies are very close to each other (as numbers/positions). Frequencies within 4 cm^{-1} are really difficult to identify experimentally, since these very small shifts are comparable with the resolution used typically in spectroscopic measurements. Therefore, in specifying the morphology of the material, careful analysis should be done by considering frequencies that do not have locations closer than the resolution of the system. Similar concepts are applicable for X-Ray analysis, too, especially that the diffraction lines broaden with confinement.

Table 1.4: Raman vibrational frequencies associated with monoclinic and orthorhombic structures of WO_3 . [45-47]

Monoclinic WO_3	Orthorhombic WO_3
33	
44	45
60	61
71	
83	77
94	91
143	143
182	179
	203
242	
	253
273	271
	303
326	
	374
638	636
716	713
806	807

Whereas structural and spectroscopic properties of WO_3 are well known, it is worth mentioning that its characteristics are also strongly dependent on the conditions and methods used in material fabrication.

1.4 PROPERTIES OF DOPED METAL OXIDES

Although some gas sensors based on oxide semiconductors have been commercialized for years, many problems still need to be solved in order to improve their 3S characteristics (e.g. sensitivity, selectivity, and stability). In the general course of enhancing the numerous applications mentioned above, scientists found other unique properties of metal oxides while experimentally doping with different metals or mixing various metal oxide materials. From that point on, numerous research projects were undertaken and experiments were performed to increase the range of useful sensor properties. The findings listed below provide further relevant examples of studies that were carried out to detect various gases under various conditions.

Whereas many doping materials have been tried to enhance selectivity because, under humid conditions or in a high water vapor environment, detection capability goes down drastically, no comprehensive understanding on how the doping process would benefit the sensitivity and selectivity is yet available and the subject is in need of further studies. Therefore, understanding from a microscopic perspective the doped material properties is essential.

The sensitization mechanisms are categorized into two parts – chemical and electronic sensitization.[48] The process of chemical sensitization is based on embedding metals or noble metals (Pt, Au, and Pd) in metal oxide materials to promote the probability of interaction with the gas to be measured. Another advantage of this process is known as remote control of the catalytic and sensing properties of the metal oxide. Basically, the presence of the noble metals increases the supply of oxygen on the surface and this can be explained by the fact that ions of oxygen molecules are released after the

reactive gas comes into contact with the surface, providing new ions, while the oxygen ions are then transferred deeper into the metal oxide. The overall resistance of the surface decreases due to extra electrons in the surface layers.[48] The process of electron sensitization is based on using fine oxidized metal particles as additives and as a result, enhancing the positivity of the n-type semiconductor, which in turn increase the base resistivity. A well known theory to explain this phenomenon is described as the activation due to electron transfer from the metal oxide to the added metal on its surface, the space-charge depth increasing, which, in turn, decreases the electron concentration on the surface layer.[48]

Wang *et al.* have extensively investigated the detection of various chemical pollutants (NO_2 , NO , NH_3) by using WO_3 doped with various metal oxides as the sensitive materials.[25] NH_3 and NO were allowed to interact with various thin films made by an aqueous soaking method. At 350°C , films of WO_3 loaded with 1 wt.% Mg, Zn, Mo and Re showed good responses to both NH_3 and NO , and were thus found to be good candidates for NH_3 and NO gas sensors. These studies also provide guidelines for discerning which dopants result in films that do not respond to NO and NO_3 . Particularly for NO measurement, WO_3 was applied to a sapphire substrate and the thin films were annealed at different temperatures ranging from room temperature (RT) to 600°C and the surface roughness was recorded, as well as the sensitivity at RT, 400°C , 500°C , and 600°C . Increasing the annealing temperature showed positive effects on the surface roughness and crystal size; the highest sensitivity was found at 500°C . The abrupt topography change at 600°C didn't accommodate the increment in sensitivity. RF reactive magnetron sputtering was used to deposit sensors, interrupting the process various numbers of times for various durations. It was concluded that for higher interruption numbers and times, smaller grain sizes are typical in the thin films. The higher values of these parameters also have positive impacts on sensitivity; the optimal interruption time exceeds 90 s.

Also, Profs. Vetelino's and Lad's groups from the laboratory for Surface Science and Technology of the University of Maine showed that the amount of the dopant influences the sensitivity

and the optimum operating temperature.[28-30] Among the various dopants of gold, platinum, or palladium, it was found that the spillover effect of Pt is larger than that of Au. More specifically, at under 1 ppm H₂S and at an operating temperature of 220°C, the individual sensitivities of the Pt and the Au-Pt doped WO₃ gas sensors are 23 and 5.5 ppm, respectively. The results show that the Pt doped WO₃ gas sensor exhibits acceptable response and recovery times, as well as a high sensitivity toward H₂S.[28-30]

Vuong *et al.* investigated the response to gas testing of crystalline SnO₂ with various crystallite grain sizes ranging between 6 and 16 nm, which were prepared by subjecting stannic acid gel to hydrothermal treatments under various conditions. Thin film sensor devices with different film thicknesses between 200 and 900 nm were fabricated to investigate sensing properties toward H₂S gas. It was found that the sensor response to H₂S was significantly enhanced with decreasing film thickness and with increasing grain size up to 16 nm. The response was surprisingly large, exceeding 104 ppm at 150°C, for the device deposited with a 200 nm thickness.[49]

Also, Gong *et al.* found that an Ag doped nanocrystalline SnO₂ gas sensing material presents better sensitivity compared to pure SnO₂, due to the distribution of Ag₂O particles in grain boundaries of nanocrystalline SnO₂ and the formation of p-n heterojunctions.[50] The H₂S measurement results indicate that the developed H₂S sensor's working temperature is about 70°C, which is much less than commercially available sensors and recently developed SMO sensors.[38] Moreover, Cu-SnO₂ composites show strong sensitivity toward H₂S detection which reaches <10 ppm of H₂S at a temperature of 100°C.[38,] Other sensors containing copper, iron, cadmium, and indium oxides were also found to be selective toward H₂S.

As illustrated above, many studies have been done to utilize metal oxide semiconductor sensors to detect H₂S, and various metal oxide materials along with inert metal doping have been tried to maximize the detectability and these works have reported the optimum temperature where it occurs.

Different grain sizes were tested and the impact of different annealing temperatures has been tested. However, not many investigations have been done to increase the operating temperature of the H₂S MOX sensor and study how the sensor would behave in such extreme conditions. As mentioned before, it is required to withstand a high temperature environment as an H₂S sensor and the temperature could reach up to 900 °C in some circumstances. Plenty of the studies have focused on increasing the sensitivity of H₂S sensors but few have investigated both high temperature sustainability and the expected changes of sensitivity that might accompany this characteristic. Our research goal is to increase the temperature range of WO₃ based MOX sensors by Ti doping. According to our literature reviews, Ti doping will delay the crystallization of WO₃ due to the added impurity and will change the ratio of W⁺⁴ and W⁺⁵ because of the different oxidation numbers of tungsten vs. titanium.

Whereas WO₃ and Ti are materials in pure forms have been investigated intensively, not many studies have been done for Ti doped WO₃ and even fewer to investigate its potential as a gas sensing material. By combining the two materials, as described above, electron sensitization is expected to result. Also, with increments in temperature, oxygen absorbates or metal oxidizers should extract electrons from the metal and the metal oxide, which will, in turn, increase the space charge depth. As a result, sensitivity enhancement is expected with increased oxygen absorbates on the surface. Due to the additional element that was added to WO₃, the crystal structure and morphology demand further investigation; the determination of various other characteristics can be anticipated along the way.

Also, it is interesting to note that the specific heat of tungsten (0.133 @20°C J/g mol) is much lower than that of titanium (0.523 @20°C J/g mol), which means that when the same amount of heat energy is applied to both materials together, unbalanced temperature distribution can occur to affect the annealing process. Also, according to Pecquenard *at al*, the lifetime of WO₃-Ti thin films can be five times longer than that of pure WO₃. [45]

Thus, the outcomes of the microscopic, structural, and spectroscopic studies, which will be presented in this work, will bring valuable insights about this material.

Chapter 2: Experimental Details

2.1 INTRODUCTORY REMARKS

Spectroscopy is, by definition, the study of the interaction of light and matter. Microscopy is the field of using microscopes to see an object that is beyond the human visibility range. The goal of this research is to analyze the crystal structure changes, with temperature variation, of WO_3 and Ti doped WO_3 . Whereas there are many ways to achieve this goal in the fields of spectroscopy and microscopy, the three methods selected for this work are atomic force microscopy (AFM), X-ray diffraction (XRD), and Raman spectroscopy. Since these techniques provide information about size distribution, structure, and crystallinity of the material studied, not only will the results obtained complement each other, but will substantiate future design options for new materials.

For example, our previous research that was conducted on pure WO_3 by using Fourier transform infrared absorption spectroscopy and X-ray photo-electron spectroscopy (XPS) for samples grown at identical substrate temperatures facilitated capturing the trend of characteristic changes associated with material morphology.[51] In addition to the crystal structure investigations, surface morphology analysis is also important to serve the end result of detailed characterizations of metal oxides. Thus, by using AFM, which has the same or even better resolution capability as Scanning Electron Microscopy (SEM), not only can direct visualization of nano-crystallites on sample surfaces be achieved, but also the surface roughness profiles can be recorded on a scale of a few nanometers.[52]

In the subsequent sections, detailed discussions of each technique and equipment that were used will be addressed. These discussions will contain brief descriptions of the fundamental principles and the originators of the equipment in order to credit them for today's advancements in material analysis and characterization.

2.2 ATOMIC FORCE MICROSCOPY (AFM)

Atomic force microscopy is a revolutionary technical field that uses a minuscule probe to measure a sample surface with very high magnification. The reported resolution is on the order of less than a nanometer. Compared with other conventional microscopic techniques, which mainly depend on interaction of light or electrons with the sample, AFM physically ‘feels’ and also records the height of the sample’s surface with the probe. It builds a 3D map of the height of the surface with resolution higher than that of a Scanning Electron Microscope (SEM).[52-54] For comparison purposes we present below, in Table 2.1, potential resolutions attainable with AFM, SEM and TEM.

Table 2.1: Comparison of resolution and capability of AFM with SEM and TEM.[52]

	AFM	SEM	TEM
Sample preparation	little or none	from little to a lot	from little to a lot
Resolution	0.1 nm	5 nm	0.1 nm
Relative cost	low	medium	high
Sample environment	any	vacuum(SEM) or gas (environmental SEM)	vacuum
Depth of field	poor	good	poor
Sample type	Conductive or insulating	conductive	conductive
Time for image	2–5 minutes	0.1–1 minute	0.1–1 minute
Maximum field of view	100 μm	1 mm	100 nm
Maximum sample size	unlimited	30 mm	2 mm
Measurements	3 dimensional	2 dimensional	2 dimensional

Also while SEM samples are limited to conductive or semi-conductive materials, AFM provides greater flexibility of sample selection. The selection ranges include, besides non-conductive materials, both very hard samples (e.g., the surface of a ceramic material or a dispersion of metallic nanoparticles), and very soft materials (e.g., highly flexible polymers, human cells, or individual molecules

of DNA). Furthermore, the advantages of AFM include minimum sample preparation requirement, no need of measurements in high vacuum environments, and low cost compared with other high resolution systems such as the scanning electron microscope (SEM) and transmission electron microscope (TEM).[52-54] Along with these flexibilities, AFM comes with three imaging modes, which will be further illustrated in detail later. Therefore, currently it is used in all fields of science including chemistry, biology, physics, materials science, and nanotechnology.[53,54]

2.2.1 Principles of AFM

AFM consists of three major components: a probe that is attached at the tip of a cantilever, a laser light, and a photodiode. The infinitesimal movement of the probe is controlled by piezoelectric materials, which expand and contract in proportion with an applied voltage. The size and geometry of a probe depends on hardness, roughness, and measurement method used. The height ranges from 1 (at the contact mode) to 8 μm (tapping mode) and at the end of the tip could reach up to a few nanometers. As illustrated in Figure 2.1, the tip moves along a set path (x, y, and z directions) of the sample surface and with the movement, depending on the surface roughness or interaction forces, the cantilever flexes up and down. By aligning the laser light reflecting off from the cantilever to the photodiode, the movement can be measured with Hooke's law ($F = kX$), which translates the height or roughness information of the specific position. In turn, the cantilever's elevation changes are controlled by the piezoelectric elements.[52-54] Thus, these three components: photodiode, cantilever, and piezoelectric movements, create a control loop to record the sample's surface morphology.

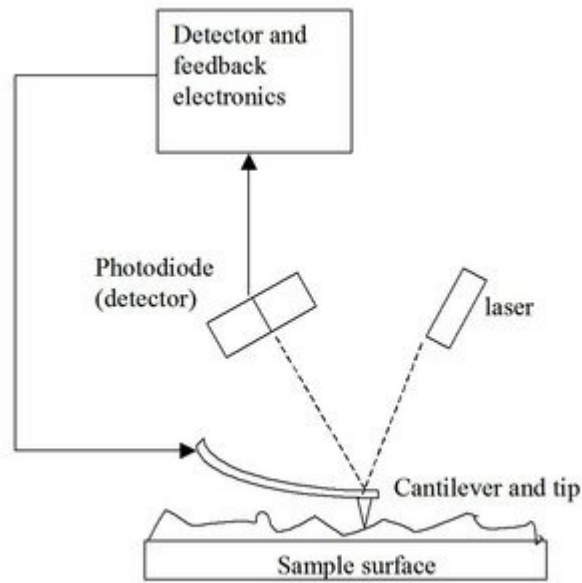


Figure 2.1: Illustration of AFM basic components and their interactions and feedback system.[53]

2.2.2 AFM Modes

AFM can be operated in two major modes depending on the hardness and roughness of the sample, as well as on the interaction forces with the sample. There is a contact and a non-contact mode. The major differences, as the names imply, involve the interaction distance between the probe and the sample. Also, for non-contact mode, the probe's behavior is controlled by various forces such as van der Waals forces, capillary forces, chemical bonding, and electrostatic forces.[52-54] On the other hand, contact mode follows the physical shape of the surface. Usually, higher resolution is expected with the contact mode. However, considering the triangular shape of tip end, it needs to be kept in mind that prolonged use of the contact mode will deteriorate the sharp edge faster than the non-contact mode. Also, using a cantilever with lower resonant frequency and stiffness is required for the contact mode compared with its counterpart. In non-contact mode, instead of being continuously dragged, the tip, which oscillates at resonant frequency, moves across the surface of the sample contour and measures the

deflection of the cantilever. Because noise and drift are expected for this measurement, a low stiffness cantilever is required to increase the signal to noise ratio. Also, considering very high attractive forces near the surface, there is a good chance that the nano-tip of the cantilever will snap into the surface.

Another major difference of the non-contact mode compared to the contact mode is that the cantilever is placed slightly above the sample surface, between 1 nm and 10 nm, where the van der Waals force is known to be dominant.[52-54] The cantilever is oscillated at a frequency slightly above its resonant frequency, where the amplitude is less than 10 nm. Thus, the decrease of the resonance frequency of the cantilever when it encounters the van der Waal force field is already considered. With the decrease of resonant frequency and the feedback loop system to keep the oscillation amplitude constant, the scanning software constructs a topographic image of the sample surface by measuring the tip to sample distance at each data point along the x and y axes. By using this mode, tip or sample degradation is radically reduced; however, the resolution of topography might need to be compensated within a few monolayers of the surface [55].

The last, but not the least mode for AFM is tapping mode. As discussed before, there are still some limitations inherent to the contact and non-contact modes. Thus, a hybrid of the two modes was created and is known as ‘tapping mode’. It is the most widely used mode in the AFM field. All of our images were generated with tapping mode, also referred as AC mode or intermittent contact mode. The tapping mode is very similar to the non-contact mode in the sense that the cantilever oscillates up and down at near its resonance frequency. However, the amplitude of this oscillation is much larger than the one of the contact mode and usually ranges between 100 and 200 nm. Within this range, not only the Van der Waals force, but also other forces such as dipole-dipole interaction, electrostatic, etc. are factors that decrease the amplitude of this oscillation as the tip gets closer to the sample.[52-55] A servomechanical (control motor) device employs the piezoelectric actuator to control the height of the cantilever above the sample and the constant adjustment which is needed to keep the same amplitude

while scanning an uneven surface. With the recording of these constant adjustments, a tapping AFM image is generated.

In AC mode, the cantilever is oscillated at its resonant frequency, with a free amplitude A_0 . While the cantilever is approaching the surface, the oscillating amplitude is damped to a value A , which depends on the distance to the surface. The ratio: [31]

$$r = A / A_0 \quad (2.1)$$

defines the damping of the amplitude while the tip is in contact with the surface and is proportional to the applied force.[5] By keeping the damping of the amplitude constant, the surface topography can be imaged. The interaction between the tip and the sample is predominately vertical, though negligible lateral forces are encountered.

In AFM AC mode, the tip is in intermittent contact with the surface. The tip hits the surface periodically at or close to the resonant frequency of the cantilever. The tip is also fully retracted from the surface at the same frequency. From these two considerations, the properties of the cantilever for AC Mode measurements can be derived. The cantilevers have to be stiffer than those for contact mode in order to detach the cantilever from the surface ($k > 1\text{N/m}$) and the resonance frequency of the cantilever should be far above the resonance frequency of any other mechanical component of the instrument, typically larger than 50kHz.[55]. The stiffness and frequency of our cantilevers are manufactured and set to 2.8 N/m and 285 kHz.

2.2.3 AFM experimental set-up

A *WITec alpha 300 RA* system (see Figure 2.2) combining both AFM and confocal Raman was used for current AFM measurements. All data were recorded using a driving amplitude of 0.052 V_{pp}, driving frequency of 57780.46 Hz, and set point of 0.8380003V. Also, P&I gains were fixed at 7% and 9%.

The surface topography of an area of $1 \times 1 \mu\text{m}^2$ was measured using 512 lines per image and 512 points per line.

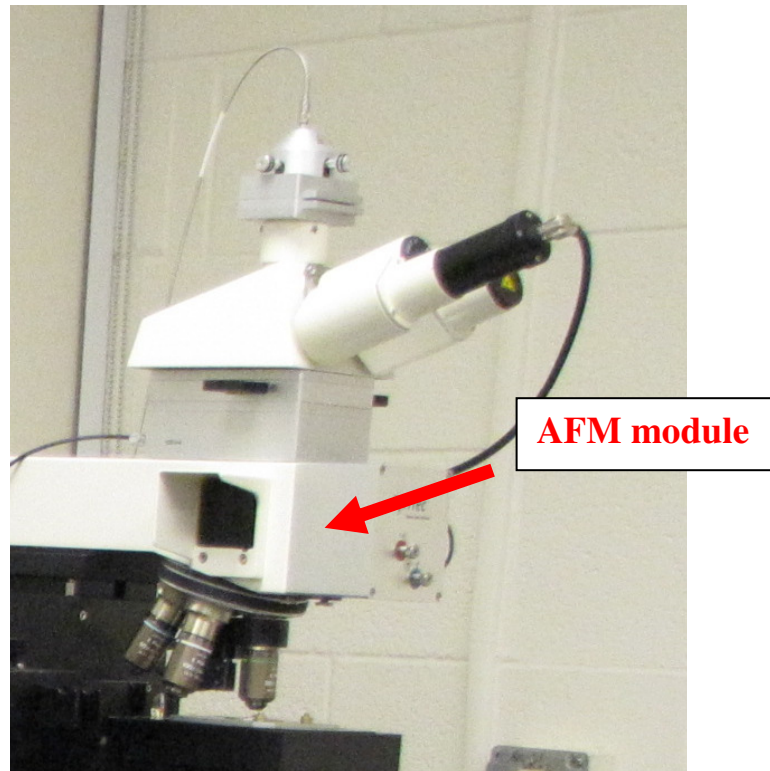


Figure 2.2: Image of *WITec alpha 300 RA* AFM module.

2.3 X-RAY DIFFRACTION (XRD)

Matter is composed of atoms. Most solid materials have a pattern or an arrangement of atoms that is configured according to the minimum energy rule and the nature of chemical bonding. An amorphous material such as glass, which is the most well known example, shows a pattern that can be detected in larger scale. The discovery of X-Ray Diffraction (XRD) was made in 1912 by a father and a son, Sir W.L. Bragg and Sir W.H. Bragg. They found that crystalline solids produced surprising patterns of reflected X-rays. By collecting, organizing, and analyzing these patterns, they postulated and

experimentally demonstrated the Bragg's law. Since then, Bragg's law has become a fundamental component of materials science research, especially for material characterization.

To understand XRD and how it can be applied, the three major components need to be explained in detail. They are: X-ray sources, Bragg's Law, and lattices & crystal structures. The subsequent sections will present information on these topics.

2.3.1 X-rays and X-ray tube

X-rays, which are produced by X-ray tubes, are high energy electromagnetic radiation. They have energies ranging from approximately 200 eV to 1MeV, which put them between γ -rays and ultraviolet (UV) radiation in the electromagnetic spectrum. Within an X-ray tube, electrons are generated by a heated cathode and will move to the water cooled wall of an anode. There, a high electric potential difference and vacuum environment will promote a high energy impact by the time they reach the anode wall. This high energy impact of electrons will produce photons, called X-rays. During this process, ideally all the kinetic energy of electrons is converted to photons. Unfortunately, in reality, most energy is dissipated by heat. There are only a few characteristic radiation lines, called $K\alpha$ and $K\beta$. For an easier comprehension of the process of producing X-rays and for direct visualization of the major components of an X-ray tube, we present in Figure 2.3 a schematic description.

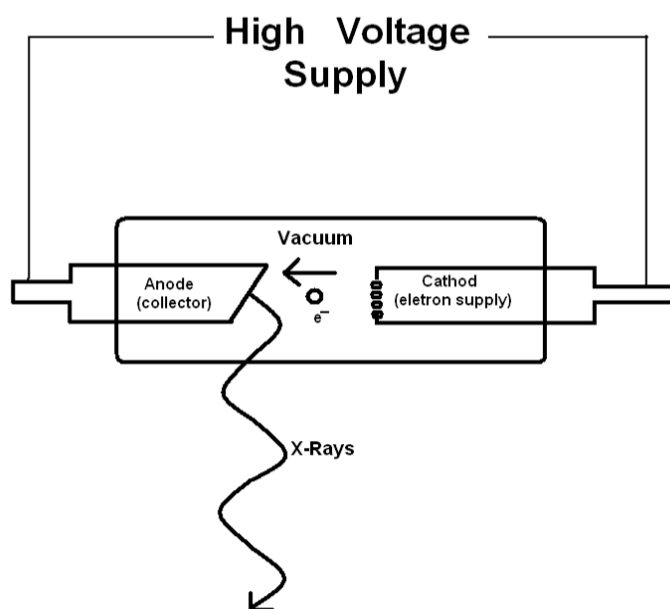


Figure 2.3 : Scheme of X-ray tube's major components and of X-ray production.

2.3.2 Bragg's Law

Once the X-rays are produced they will travel to an object to be studied. There are three possible interactions at this point – scattering, interference, and diffraction. Scattering is the process of absorption and reemission of incoming X-rays in different directions. Interference is the superposition of two or more of these scattered waves. Diffraction is the interference of scattered waves that results in constructive interference in certain directions. For XRD, we study the diffraction patterns after X-rays interact with the object. The relationship between the incident X-rays and the emitted radiation is described by Bragg's law. Before defining Bragg's law, the following four variables need to be defined:

- **n** : an integer number
- **λ** : the wavelength of incident radiation
- **d** : the spacing between atomic lattice planes
- **θ** : the angle between the incident x-ray and the lattice plane.

Also, for easier visualization of these variables, as well as their roles in the interaction between the radiation and the matter, from which Bragg's law was discovered, we present in Figure 2.4 a schematic diagram of this process.

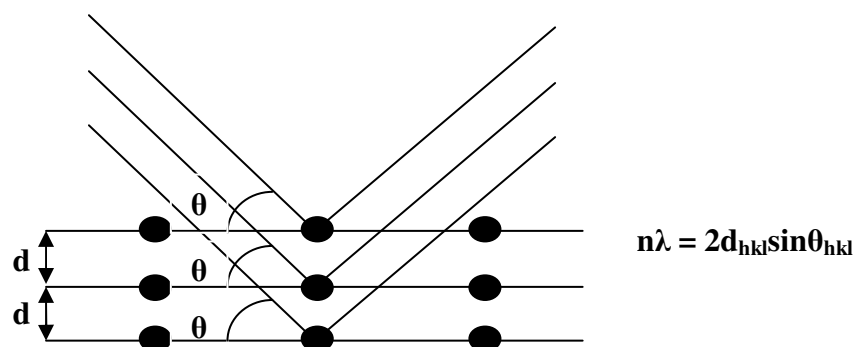


Figure 2.4: Bragg's law and its parameters.

By using Bragg's law, one can determine **d**, the spacing between atomic lattice planes. This can be obtained from knowing the wavelength of incident radiation (by design of the x-ray source), measuring different incident angles, and observing the diffraction pattern. In addition, the orientation of a single crystal as well as the degree of preferential orientation can be also determined by studying diffraction patterns while rotating a sample. In this context, XDR is a well known to be a very useful technique for finding the crystal structures of unknown samples, as well as for analyzing stresses in small crystallites.

2.3.3 Lattices and crystal structures

Lattices and crystal structures constitute the last fundamental topic that needs to be clarified order to have a complete understanding of XRD analysis. Solids can be divided into three categories: single crystal, polycrystalline, and amorphous. For XRD purposes, only single and polycrystals are suitable for investigation. A crystal is a solid material that shows repeated patterns or some order of arrangement in its parts such as atoms, molecules, or ions in all three spatial dimensions. If any pattern

exists, it can be described by locating identical groups of atoms or ions identically with respect to different lattice points that form a regular array with their positions all defined with respect to a common origin. The entire lattice is thus made up of repetitions of a basic array of lattice points called a unit cell. The shape and size of the unit cell determine its geometric characteristics, which are quantified by its so-called lattice parameters. The symmetry properties of ideal three dimensional lattices limit their possible types to a finite number.[6-9] These types are classified according to the 14 types of Bravais lattices, which, in turn, can each be classified as belonging to one of the seven crystal structure systems, with unit cell structures as indicated Figure 2.5 and Table 2.2 (in which a, b, and c represent the lengths of the three mutually intersecting unit cell edges, and alpha, beta, and gamma represent the respective angles between the pairs of edges of lengths b and c, c and a, and a and b), respectively.

- **Cubic:** $a = b = c,$ $\alpha = \beta = \gamma = 90^\circ$
- **Tetragonal:** $a = b \neq c,$ $\alpha = \beta = \gamma = 90^\circ$
- **Orthorhombic:** $a \neq b \neq c,$ $\alpha = \beta = \gamma = 90^\circ$
- **Hexagonal:** $a = b \neq c,$ $\alpha = \beta = 90^\circ, \gamma = 120^\circ$
- **Monoclinic:** $a \neq b \neq c,$ $\alpha = \gamma = 90^\circ, \beta \neq 90^\circ$
- **Triclinic:** $a \neq b \neq c,$ $\alpha \neq \beta \neq \gamma \neq 90^\circ$

Table 2.2: The Seven Crystal Systems

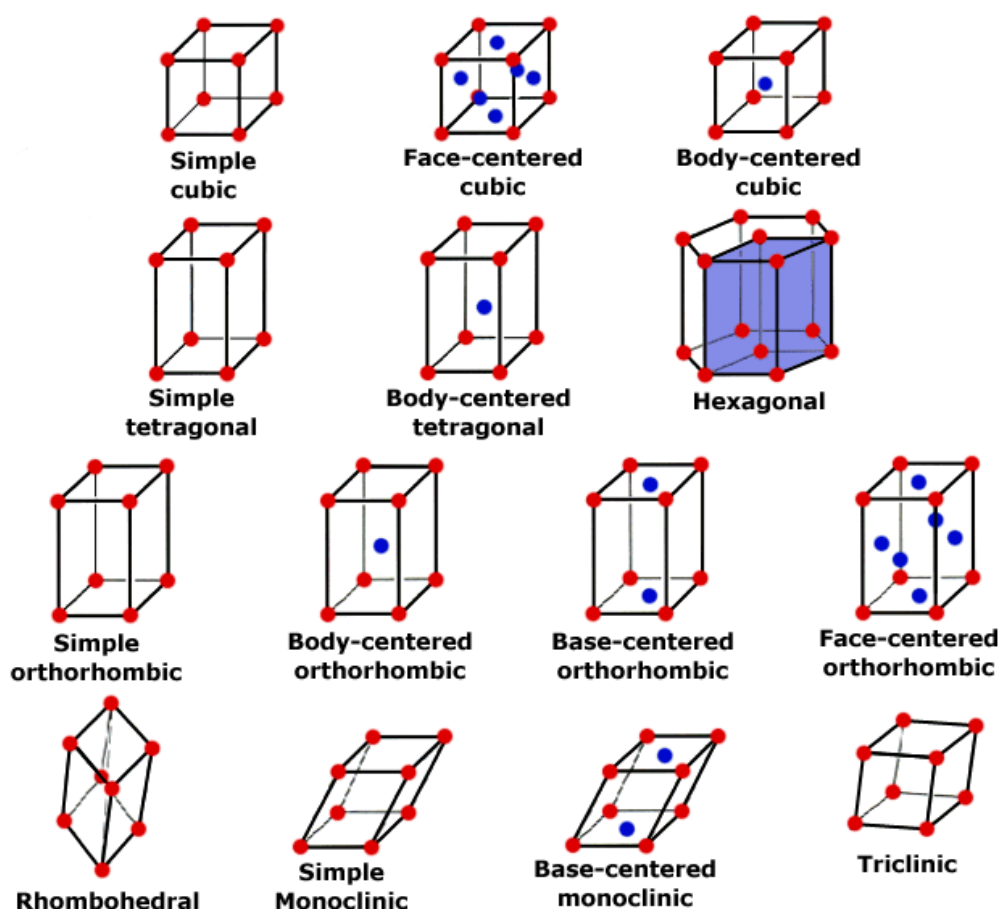


Figure 2.5: Schematic representation of the 14 Bravais lattices.[56]

So far, the discussions have focused on where there is significant diffraction pattern intensity when X-rays scatter from an object and the fact that there is a finite number of possible ideal crystal structures. Taking the finite extent of real crystals into account, crystal structure can be determined in practical situations. The latest advantages of computer development and increased data storage capacity enhance this capability. Most software that comes with an XRD system has a data base and a user friendly interface to match diffraction patterns to crystal structures. Also, XRD has other advantages which include minimum sample preparation time and high accuracy in finding d space parameters. As important examples of applications, XRD studies have been done to investigate the changes of the

crystalline behavior of a material with temperature or electric field variations, as well as for observing how deformations impact the crystalline structure.[57,58]

2.3.4 XRD experimental set-up

For our research, a Bruker D8 Advance X-ray diffractometer, which is illustrated below in Figure 2.6 has been used.

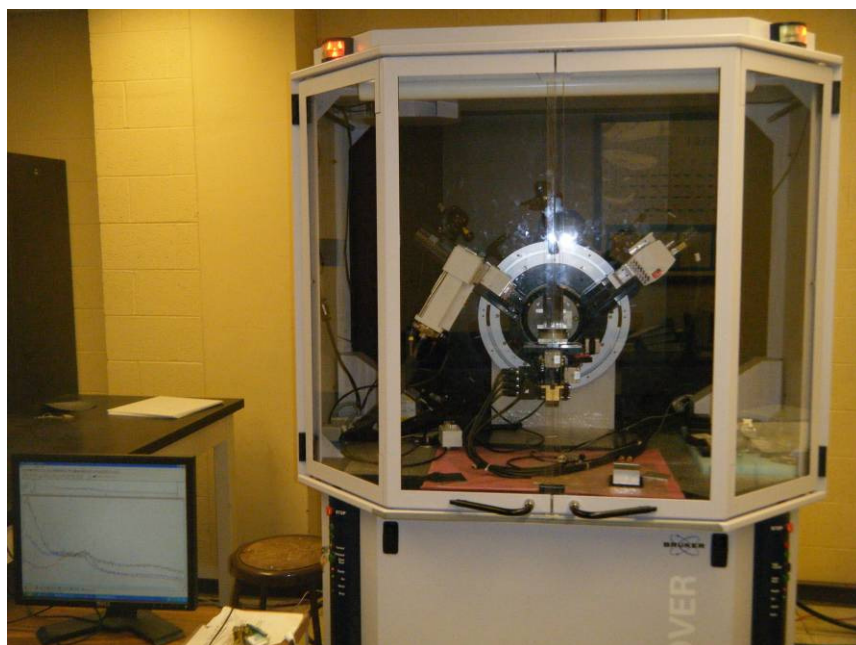


Figure 2.6: Bruker D8 Advance X-ray diffraction system.

2.4 RAMAN SPECTROSCOPY

Sir C. V. Raman discovered what is now called the Raman scattering phenomenon that is based on the inelastic scattering of photons while interacting with matter or sample. Mostly light is scattered elastically but a very small fraction of light (approximately 1 in 10 million photons) interacts with

matter. Due to this interaction, the incident light changes its original energy, frequency, and wavelength. The outcome of this change is called Raman scattering. To measure this inelastic scattering, monochromatic light, in most cases laser light, is used as a source which is directed onto the sample surface. Photons with emitted frequencies characteristic of the inelastic scattering are collected and analyzed. Filters are used to dramatically reduce the intensity of the strong laser light at its frequency as well as the unwanted elastic scattering, which has the same frequency as the unscattered laser light.[50,61]

During the inelastic interaction, the frequency/photon energy of the scattered light changes by exchanging energy with the molecules that constitute the material under study in a way that depends on the vibrational frequencies of the molecules. This process creates what is called ‘anti-Stokes scattering’ or ‘Stokes scattering’, where the final energy of the emitted light is greater or less than the incident light energy, respectively. This shift in frequency/energy gives information about vibrational, rotational, and other frequency transitions associated with the molecules. The quantum of energy of these molecular vibrations is called the phonon.[50,61] It is worth noting that Raman scattering takes less incident energy compared with fluorescence processes. Raman spectroscopy is also known as an effective technique for studying multi-component molecules. To determine crystal morphology, quantitative and qualitative studies can be combined, since not only frequency shifting information, but also the intensity, at specific wavelengths, of the light scattered inelastically from molecules can be measured using the Raman technique. Nowadays, Raman spectroscopy plays a crucial role in the analysis of an enormous variety of samples such as polymers, thin films, semiconductors, pharmaceuticals, fullerenes, and other carbon-based nano-materials.

Raman scattering can be explained in two ways: a classical approach and a quantum approach.

2.4.1 Classical approach

For a vibration to be considered as part of the Raman effect, a change of the polarizability of the molecule(s) must occur. A detailed explanation of this process is as follows: when the electric field of the electromagnetic radiation (light) is interacting with a sample, it will induce a dipole moment. This induced dipole moment (in a vector form) and the electric field are related by a property called polarizability, as described by the relation below:[60,61]

$$p = \alpha(Q) \cdot E = \alpha(Q) \cdot E_0 \cos(\omega_L t) \quad (2)$$

where the dipole moment \mathbf{p} is related to both the polarizability α and the electric field \mathbf{E} . The electric field can be exemplified as a cosine function with maximum amplitude \mathbf{E}_0 and the light's angular frequency ω_L , the latter determining the period.

Also, polarizability, which is a tensor dependant on the vibrational coordinate \mathbf{Q} , is a measure of the deformability of the electron cloud of the molecule by the incident electric field. The vibrational coordinate \mathbf{Q} depends on the molecular vibrational angular frequency ω_M as follows:

$$Q = Q_0 \cdot \cos(\omega_M t) \quad (3)$$

Thus, the change in polarizability gives rise to amplitude modulation at certain frequencies of the induced dipole moment oscillation, which, subsequently, gives rise to the Raman frequency components.[10,11] This statement is easier understood by performing a Taylor series expansion of polarizability as presented below:

$$\alpha = \alpha_0 + \left[\frac{\partial \alpha}{\partial Q} \right] \cdot Q + \dots \quad (4)$$

If this polarizability expansion is substituted into the expression of the induced dipole moment (Eq. (2)) and only the first terms are retained the following expressions are obtained:

$$p = \alpha_0 \cdot E_0 \cos(\omega_L t) + \left[\frac{\partial \alpha}{\partial Q} \right] \cdot Q_0 \cdot E_0 \cos(\omega_M t) \cdot \cos(\omega_L t) \quad (5)$$

$$p = \alpha_0 \cdot E_0 \cos(\omega_L t) + \left[\frac{\partial \alpha}{\partial Q} \right] \cdot \frac{Q_0 \cdot E_0}{2} \{ \cos[(\omega_L - \omega_M)t] + \cos[(\omega_L + \omega_M)t] \}$$

To approximate the value of \mathbf{p} , only the first two terms in the Taylor series expansion are necessary. The first term in this expression for the induced dipole moment (Eq. (5)) has the frequency of the scattered light the same as that of the incident light. Thus, this term describes what is called Rayleigh scattering or elastic scattering. The second term is for the scattered light at lower and higher frequencies than the incident light, and their respective effects are called Stokes and anti-Stokes scattering.

2.4.2 Quantum approach

Raman scattering can also be described by using quantum theory, which is schematically presented in Figure 2.7.[60,61] The incident light energy excites the molecule from ground state to a virtual state. The electron in this virtual state does not stay for long and immediately goes back to a lower energy state.

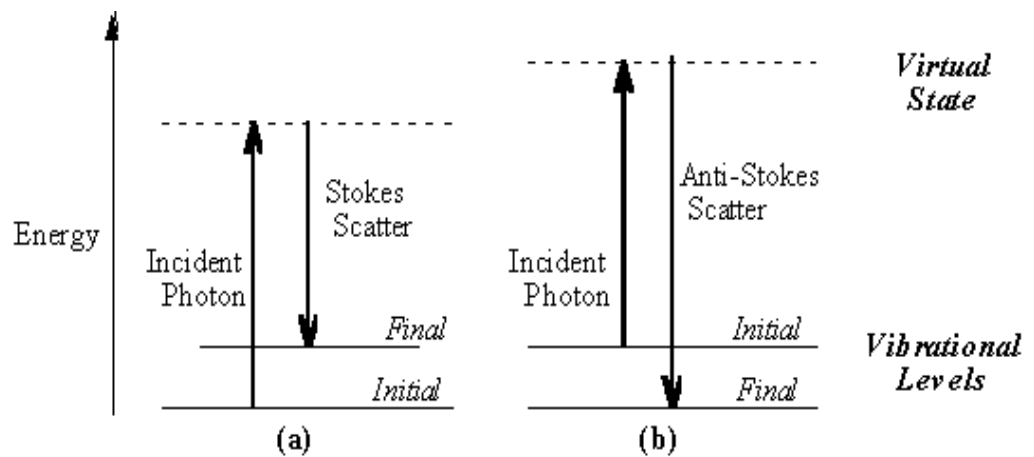


Figure 2.7: Two types of Quantum Raman scattering – Stokes and Anti-Stokes [60,61]

The calculation of the Raman frequency shift is given by:

$$\frac{\Delta\omega}{2\pi c} = \left(\frac{1}{\lambda_L} - \frac{1}{\lambda_S} \right) \quad (6)$$

where c is the speed of light in a vacuum, $\Delta\omega$ is the Raman shift, λ_L is excitation wavelength, and λ_S is the Raman scattered wavelength. For inelasting scattering, two distinctive processes are expected to occur:

- (1) A photon with angular frequency ω_L excites a molecule, which absorbs a portion of the light energy and emits a scattered photon with energy less than that of the absorbed one. The absorbed energy amount and consequently the energy difference are related to the angular frequencies by $\omega_L - \omega_M$. This shift in frequency is known as the Stokes shift.[60,61]
- (2) A photon with angular frequency ω_L is absorbed by an already excited molecule, which will give to this molecule the capacity to emit light of photon energy higher than that of the absorbed one. The resulting scattered light's angular frequency is $\omega_L + \omega_M$. This shift in frequency is known as the anti-Stokes shift.[60,61]

As mentioned before, 1 in 10 million is the chance of getting Raman scattering. Because most incident light is scattered elastically, it is essential to filter Rayleigh scattered light out in order to better capture the Raman scattering signal.[60,61] To obtain high quality Raman spectra, besides the use of high-resolution detectors, other instruments such as notch filters, tunable filters, laser stop apertures, and double and triple spectroscopic systems are employed to reduce the Rayleigh scattering.[61]

2.4.3 Raman experimental set-up

For our measurements an *alpha 300 WITec* confocal Raman system was used to enhance

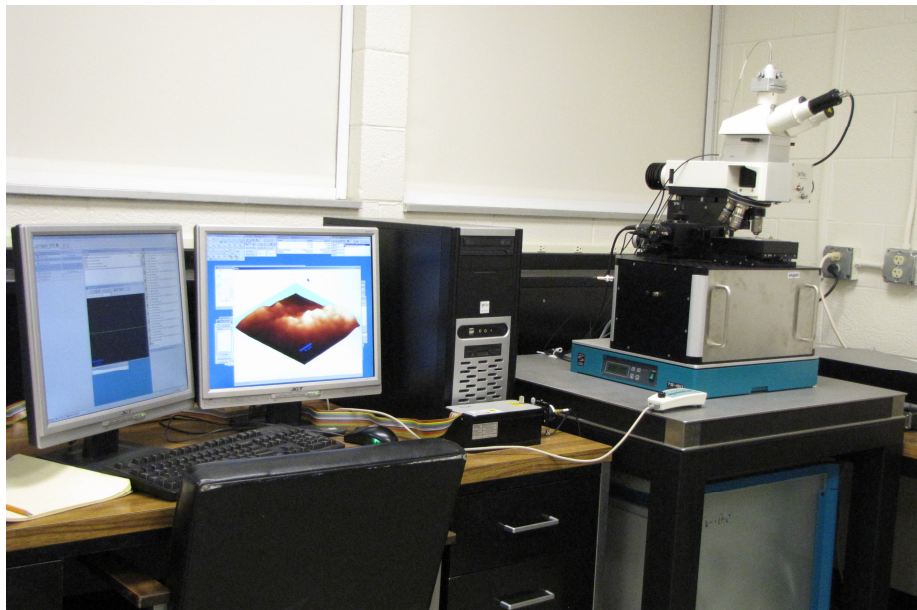


Figure 2.8: *alpha 300 WITec* confocal Raman system.

the resolution by concentrating the light on a smaller exposed area. The Raman measurements were recorded using the 532 nm excitation of a Nd:YAG laser and a 20X objective. The system available in the Optical Spectroscopy and Microscopy Laboratory is shown in Figure 2.8.

2.5 SAMPLE PREPARATION

The samples were synthesized in Dr. Ramana's Laboratory at UTEP. WO_3 and $\text{W}_{0.95}\text{Ti}_{0.05}\text{O}_3$ thin films were deposited by radio-frequency (RF) (13.56 MHz) magnetron sputtering onto sapphire and

quartz substrates, respectively, in a reactive O₂-Ar atmosphere. For the growth of the WO₃ set of samples a W metal target (Plasmaterials, Inc.) of 99.95% purity and 3” diameter was employed. The W_{0.95}Ti_{0.05}O₃ thin films were obtained by using a 2” diameter custom made W-Ti alloy-target (Plasmaterials Inc.) with a 95-5 (at % weight). The substrates were thoroughly cleaned with isopropyl alcohol and dried with nitrogen before introducing them into the vacuum chamber, which was initially evacuated to a base pressure of $\sim 10^{-6}$ Torr.

In both scenarios the targets were placed at a distance of 8 cm from the substrate. A sputtering power of 40 W was initially applied to the targets while introducing high purity argon (Ar) into the chamber to ignite the plasma. Once the plasma was ignited the power was increased to 100 W and oxygen (O₂) was released into the chamber for reactive deposition. The sputtering atmosphere consisted of Ar-O₂ mixed gases and their flow rates were controlled with MKS mass flow meters to provide an optimum Ar:O₂ flow ratio of 1:6 for the deposition of WO₃ samples and a flow ratio of 1:9 for the deposition of W_{0.95}Ti_{0.05}O₃ samples.

Also, before each deposition, targets were pre-sputtered for 10 minutes using Ar alone with the shutter above the gun closed. In order to understand the effect of temperature on the microstructure, the substrate growth temperature was varied from room temperature (RT) to 500 °C, in increments of 100°C. Deposition temperatures at the substrates were set by heating the substrates with halogen lamps and controlled with an Athena X25 temperature controller.

Chapter 3: Results and Discussion

3.1 INTRODUCTORY REMARKS

In this study we attempted to find confirmation that the growth temperature influences the roughness, the mean grain size of the nanoparticles on the surface layer of the WO_3 and Ti-doped WO_3 thin films, and the crystallinity of the material. Therefore we pursued microscopic, structural, and spectroscopic analysis by atomic force microscopy (AFM), which provides information about the first two issues, and by X-Ray diffraction (XRD) and confocal Raman scattering, which gives information about the crystallinity of the metal oxide.

Since with doping the morphology of the WO_3 samples could change, we investigate by a comparative approach, using XRD and Raman spectroscopy techniques to look for such changes when Ti(5%) and Ti(20%) doping are each applied. Furthermore, to see if there were any microstructure changes, we also performed annealing of the amorphous samples (the ones grown at room temperature) in an open furnace. The samples were annealed at 600 °C and 900 °C. We characterized these last samples by Raman scattering and infrared absorption spectroscopy. All the outcomes of these analyses are presented below.

3.2 ATOMIC FORCE MICROSCOPY RESULTS FOR WO_3 THIN FILMS

It is obvious from the AFM image of the WO_3 film deposited at room temperature, which is presented in Figure 3.1 (a), that this sample is amorphous. The roughness of the surface is about 2 nm, as revealed by Figure 3.1(b).

Figures 3.2 (a) and (b) show the AFM image and the roughness profile, respectively, of the WO_3 sample grown at a substrate temperature of 100 °C. There are slight increases in the sizes of the film

surface grains, increases that indicate the material is beginning to crystallize. Also, with increasing substrate growth temperature the surface roughness increases too, to a value of 4 nm, as seen in Figure 3.2 (b).

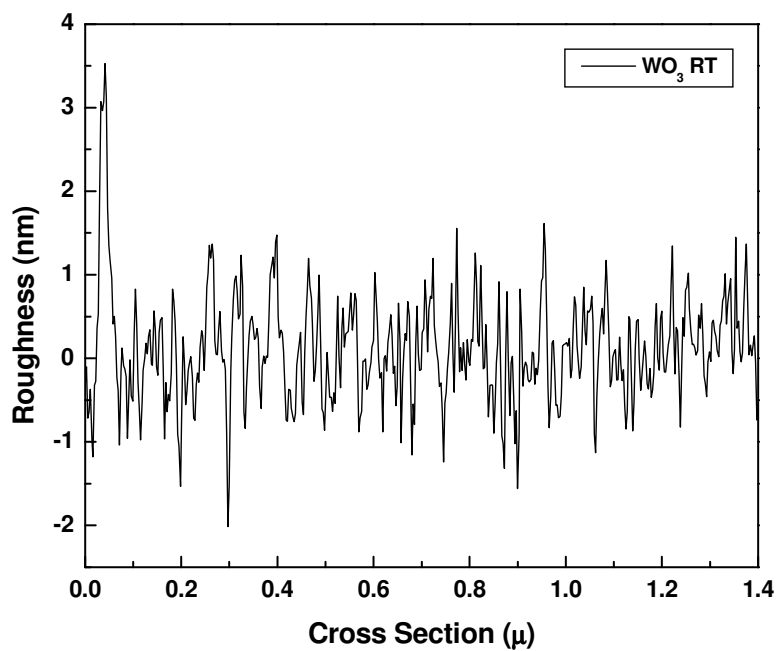
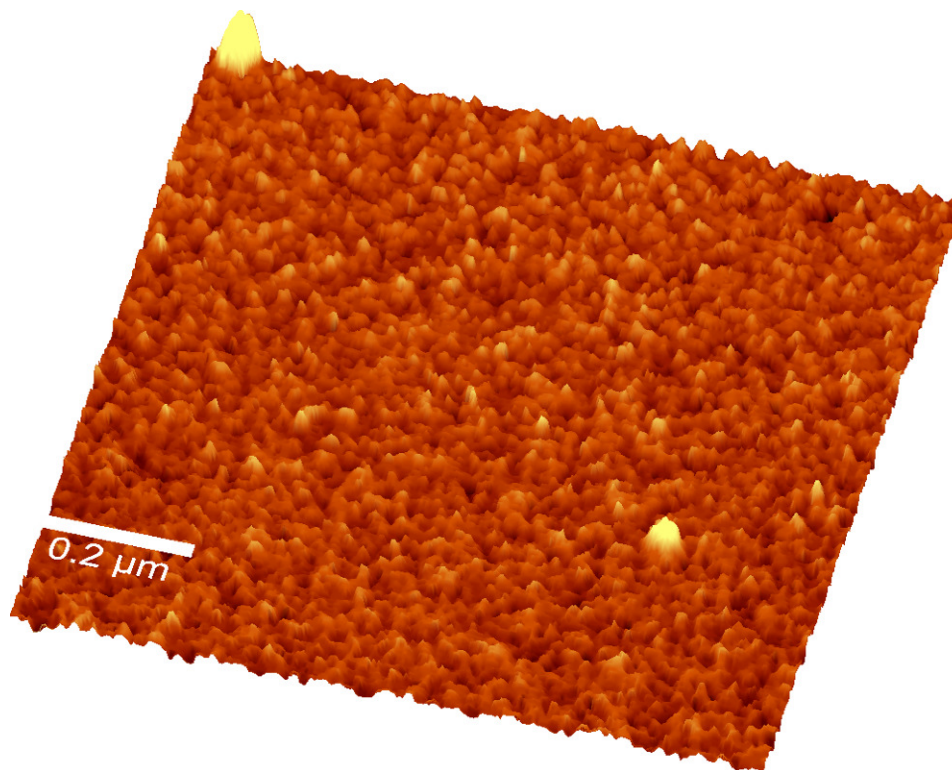


Figure 3.1: (a) AFM image and (b) roughness profile of WO₃ grown at room temperature.

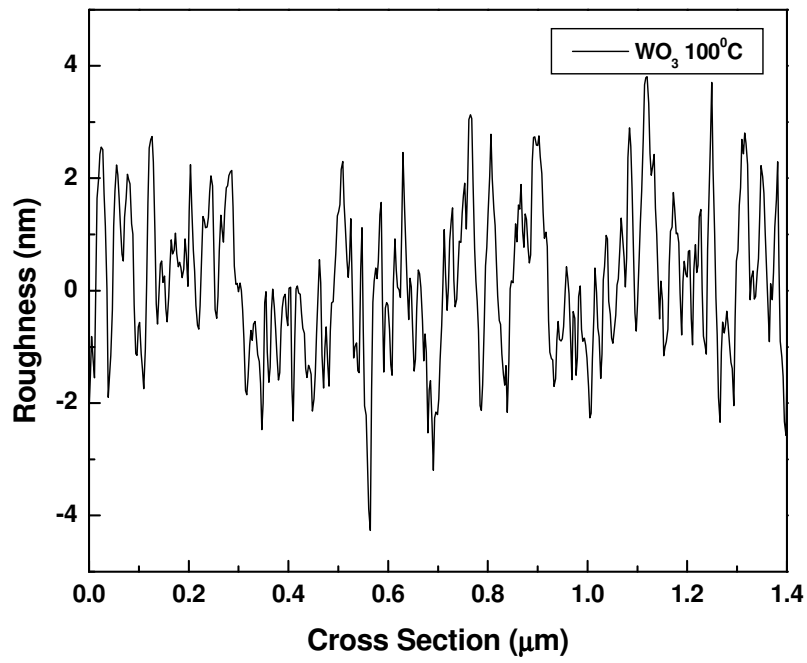
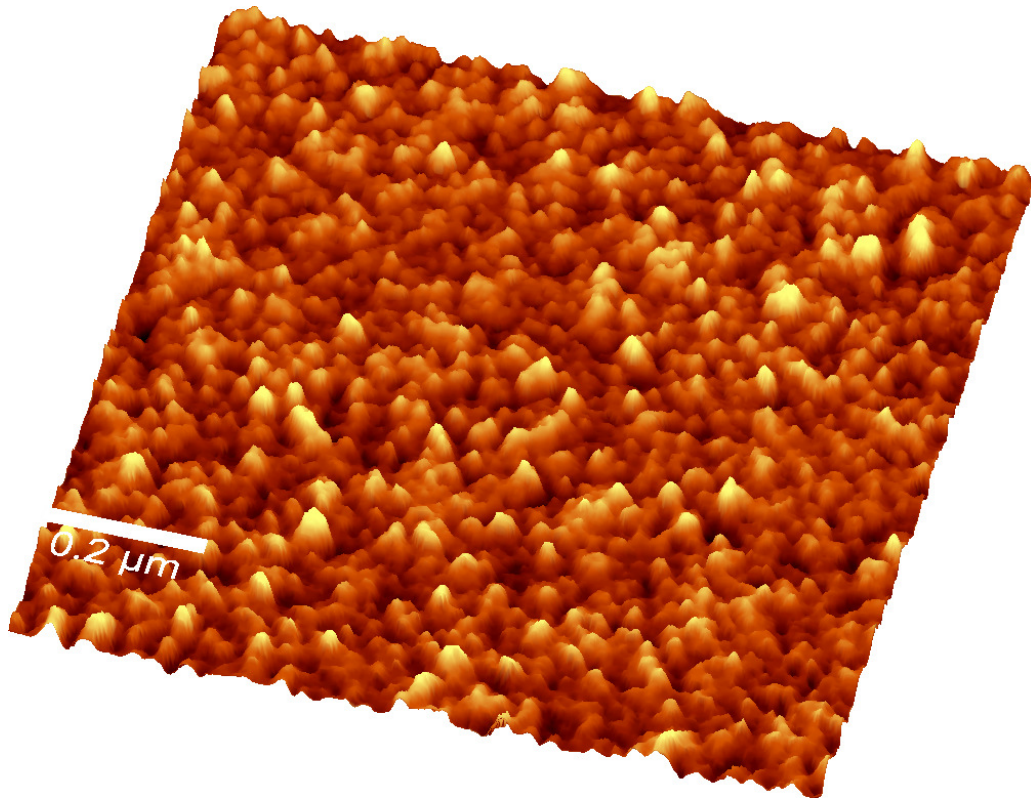


Figure 3.2: (a) AFM image and (b) roughness profile of WO_3 grown at a substrate temperature of 100°C .

The AFM images shown in Figures 3.3(a), 3.4(a), and 3.5(a) indicate the surface morphology evolution in WO₃ thin films as a function of substrate temperature, for 300 °C, 400 °C, and 500 °C, respectively. This effect is remarkable, with obvious increase in the crystallinity of the samples, especially at higher growth temperatures. As is evident from these images, the AFM data of WO₃ films can be divided into two categories where the morphology differences are significant. The first category contains the set of WO₃ films grown at temperatures ≤ 300 °C (Figures 3.1(a) and 3.2(a)). The second is the set of WO₃ films grown at temperatures > 300 °C (Figures 3.3(a), 3.4(a), and 3.5(a)). No features can be seen for WO₃ films grown at RT even at this high magnification (Figure 3.1(a)).

The increase in crystallinity of the samples with increasing growth temperature can be explain as follows: if the temperature is low so that the period of the atomic jump process of adatoms on the substrate surface is very large, then the condensed species may remain stuck to the regions where they land, thus leading to an amorphous film as seen, in this case, for the WO₃ film. The adatom mobility on the surface increases with increasing temperature. Consequently, small, isolated particles, almost spherical in their shapes, can be noticed in the above AFM images for WO₃ films grown at 100 - 300 °C (see Figures 3.2(a) and 3.3(a)). While these images show a fine, almost uniform microstructure distribution with an average particle size of 10-14 nm, the increase in temperature results in particle sizes > 30 nm. The greatest average particle size (60 nm) is measured for WO₃ films grown at 500 °C. It can also be seen in Figures 3.4(a) and 3.5(a) that the distribution of particles becomes random at high temperatures.

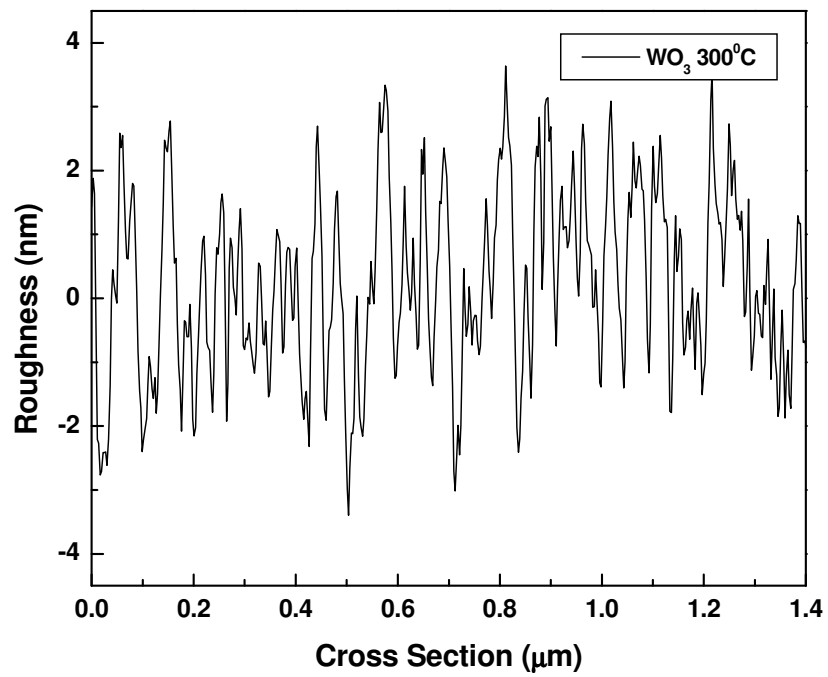
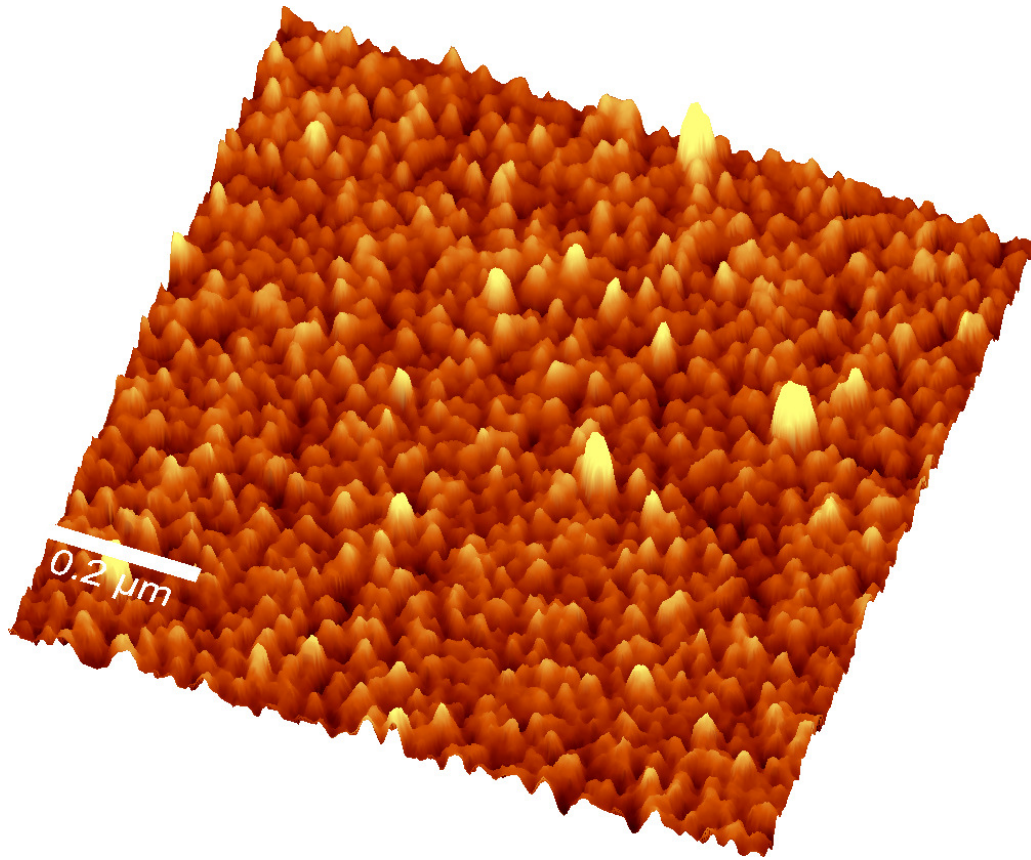


Figure 3.3: (a) AFM image and (b) roughness profile of WO_3 grown at a substrate temperature of 300°C .

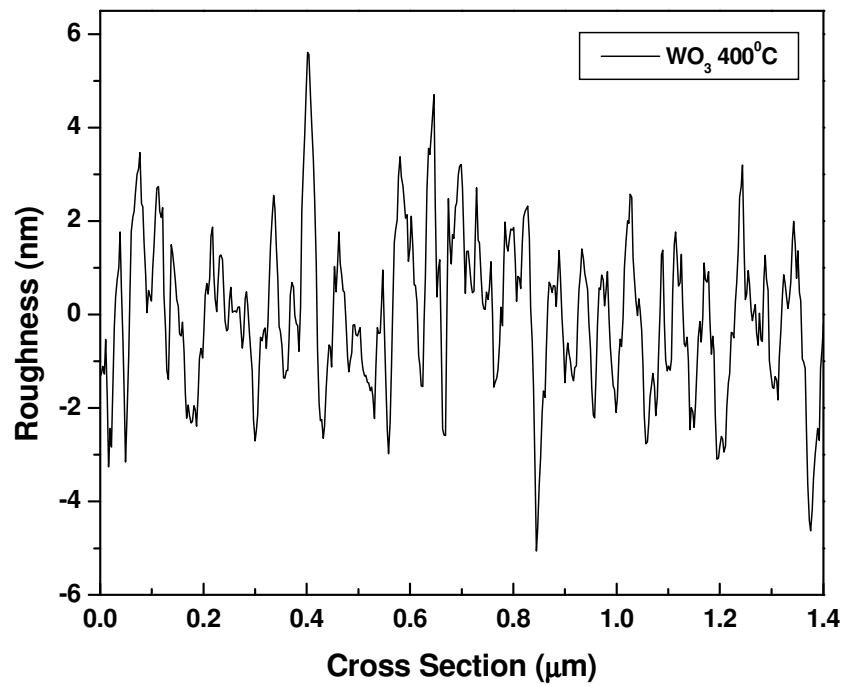
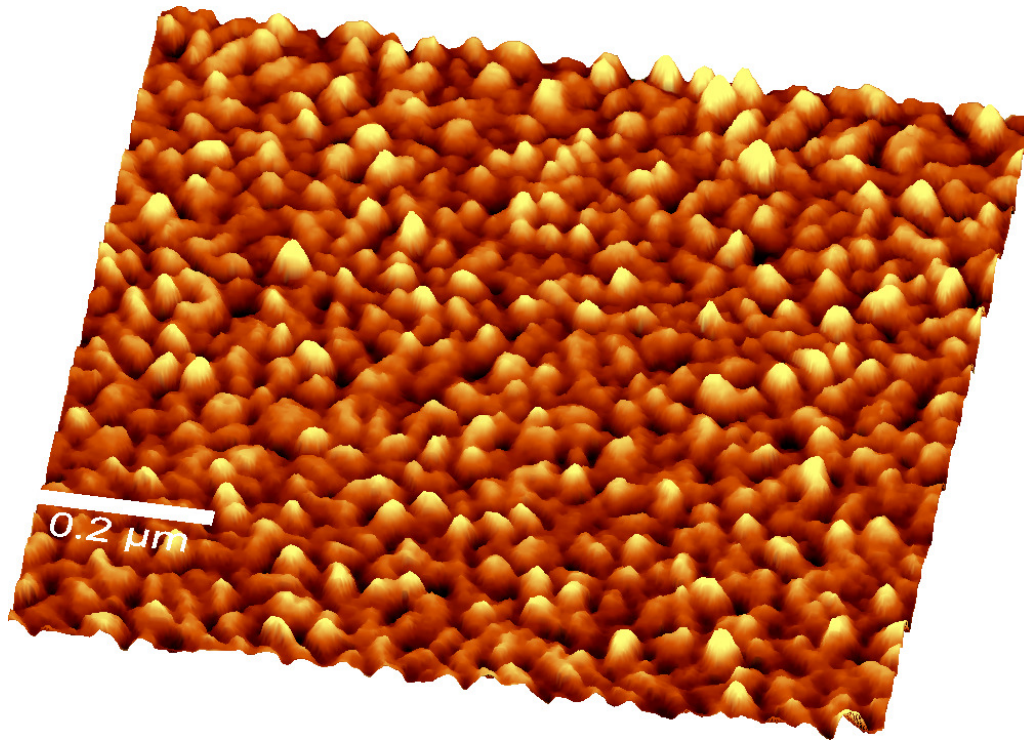


Figure 3.4: (a) AFM image and (b) roughness profile of WO_3 grown at a substrate temperature of 400 °C.

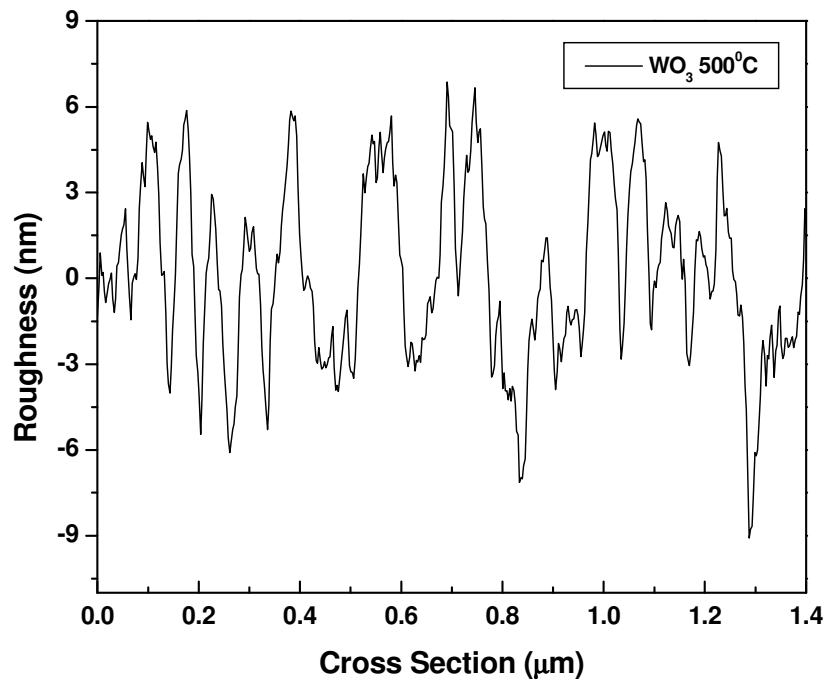
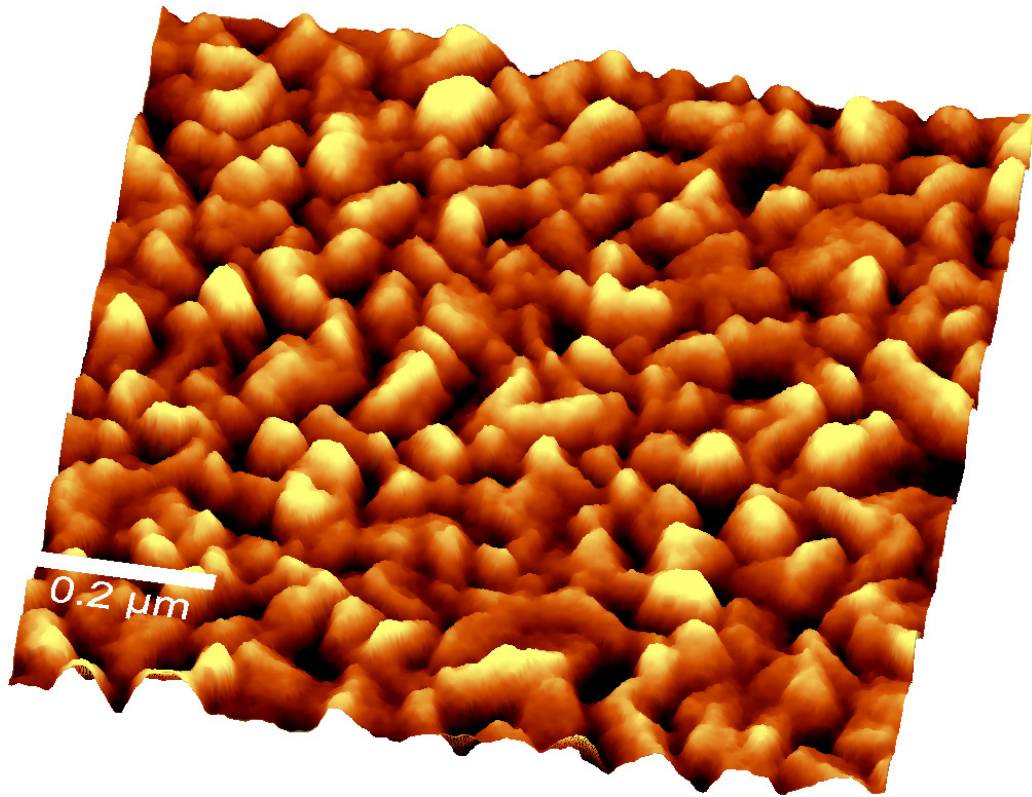


Figure 3.5: (a) AFM image and (b) roughness profile of WO_3 grown at a substrate temperature of 500 °C.

Furthermore, the almost spherical morphology noticed for WO₃ films grown at ≤ 300 °C also changes with an increase in temperature above 300 °C.

Not only is an increase in the average particle size with increasing growth temperature observed, but also the surface roughness is greater, as seen from Figures 3.1 – 3.5 (b). If for a growth temperature of 25 °C (room temperature) the WO₃ film has a roughness of 2 nm, at a growth temperature of 500 °C the roughness becomes 8 nm. The graphical relationships between the average particle size (L) and the surface roughness as functions of growth temperature are shown in Figure 3.6 (a) and (b), respectively.

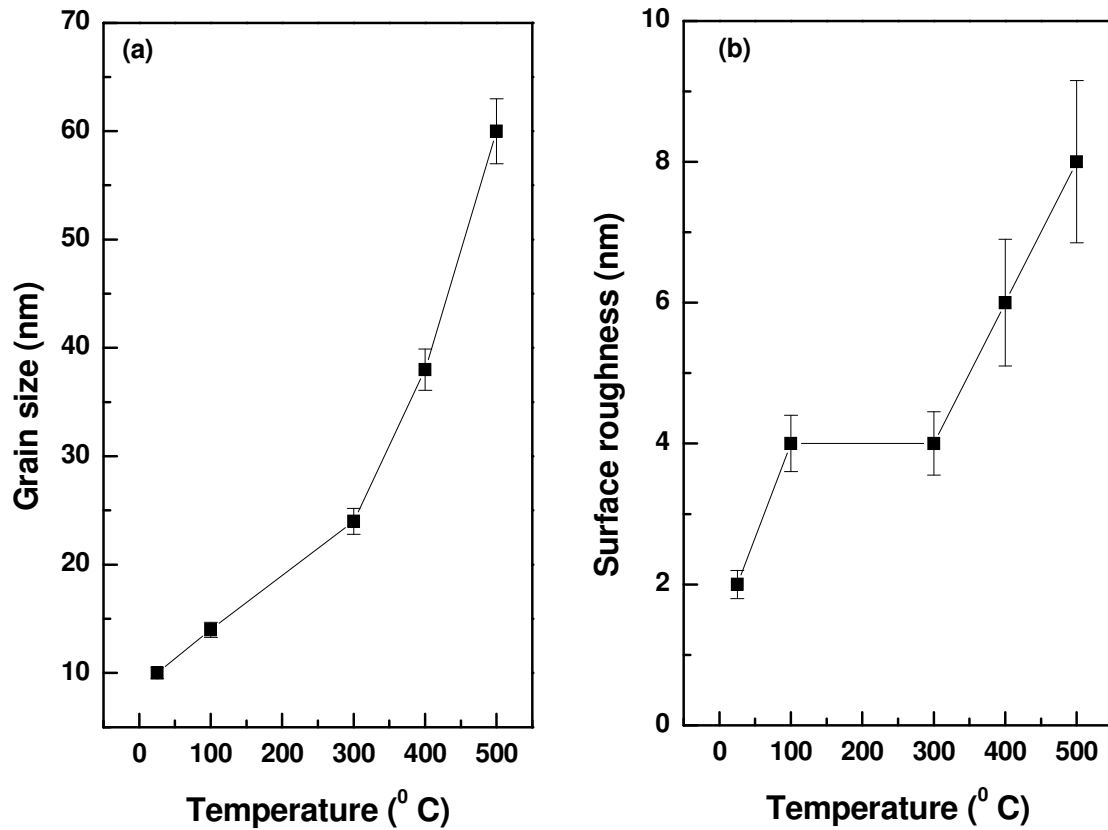


Figure 3.6: (a) Grain size and (b) surface roughness versus temperature for WO₃ films.

3.3 ATOMIC FORCE MICROSCOPY RESULTS FOR Ti(5%) DOPED WO₃ THIN FILMS

The AFM topography images for W_{0.95}Ti_{0.05}O₃ samples, which were grown using temperature conditions identical to those applied to the WO₃ thin films are presented in Figures 3.7(a) – 3.11(a). Comparison of these images with previously analyzed WO₃ samples shows that a higher temperature of at least 300 °C is required to obtain crystalline microstructure for Ti-doped WO₃ films than for WO₃ films.

Since no definite grain features can be observed in the AFM image of the sample grown at a substrate temperature of 100 °C (see Figure 3.7(a)), for a lower growth temperature such as room temperature (RT), there would be an even higher probability for this sample to be amorphous, too. Therefore, we do not present here the RT AFM image.

Also, for crystalline samples, a smaller average size of Ti-doped WO₃ nanoparticles is obtained, at the same high temperatures, than for undoped WO₃ materials, *e.g.*, at a substrate temperature of 500 °C the average size observed in the image of the W_{0.95}Ti_{0.05}O₃ sample is ~30 nm as compared to the value of ~60 nm seen for the AFM image of the undoped sample.

These observations imply a disordering effect induced by the Ti-doping on the microstructure and grain-distribution characteristics of WO₃. A reason for this observed behavior is the fact that in this case Ti occupies interstitial sites in the substitutional process in the WO₃ structure which is not typically encountered for doping elements [62]. Thus, no ordered phase of W-Ti-O mixed oxide has yet been reported in the literature.

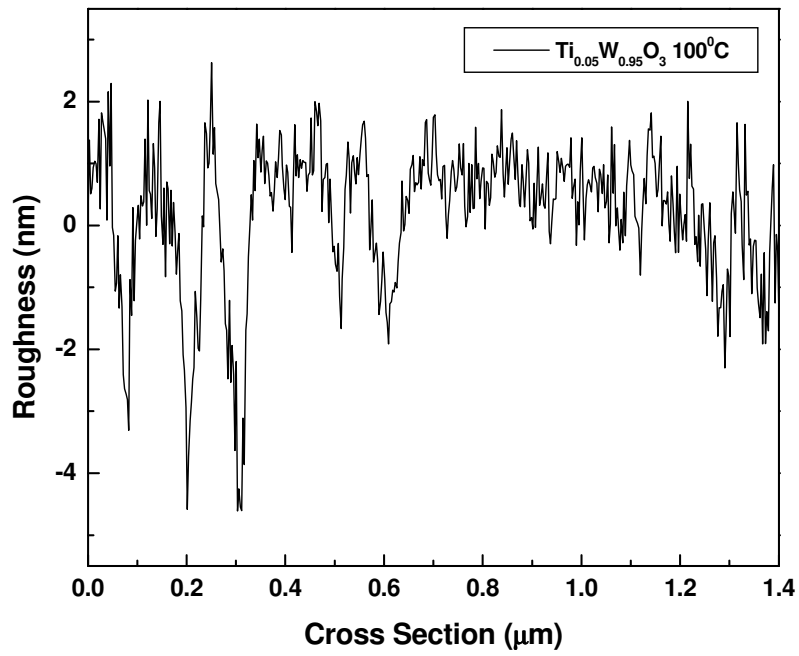
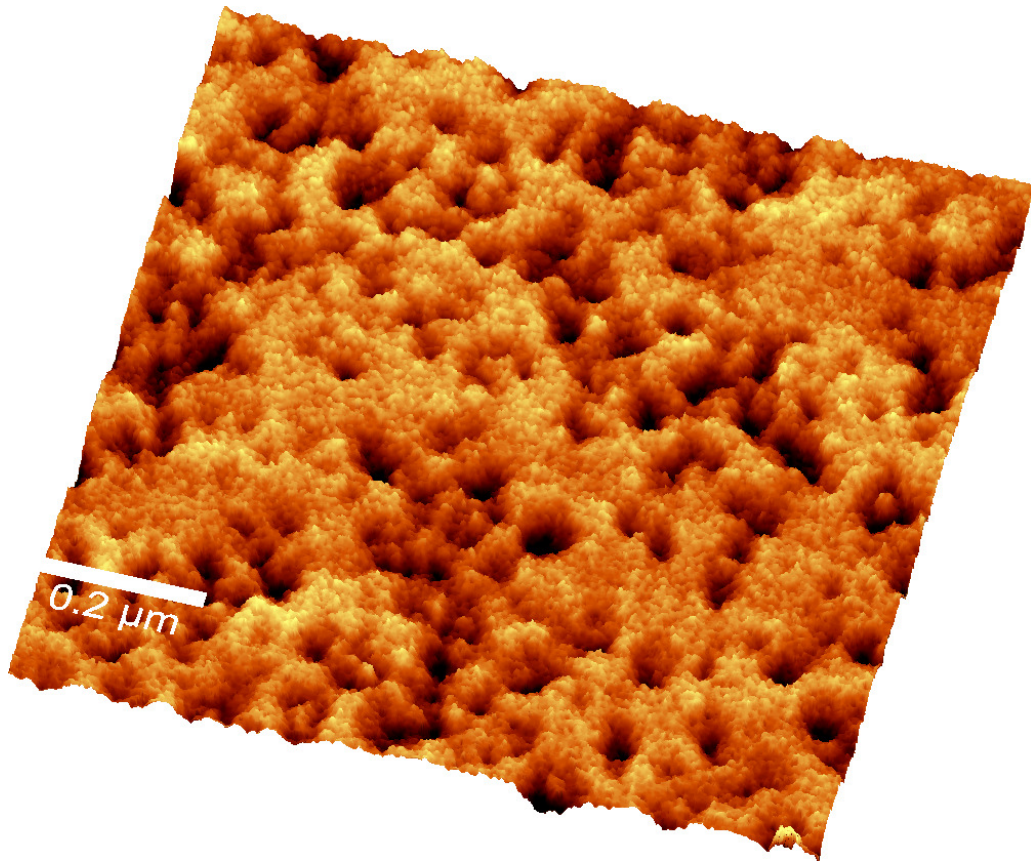


Figure 3.7: (a) AFM image of Ti (5%) doped WO₃ grown at a substrate temperature of 100 °C.

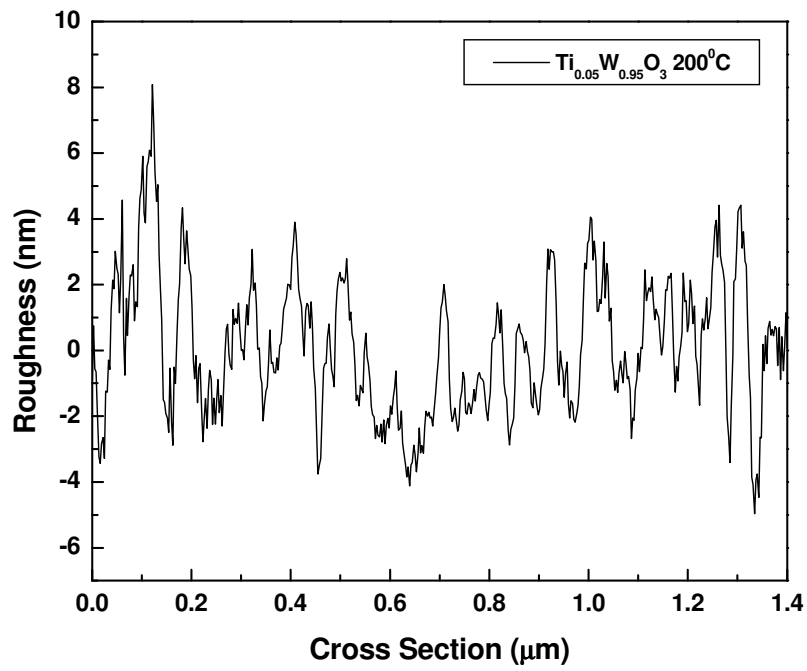
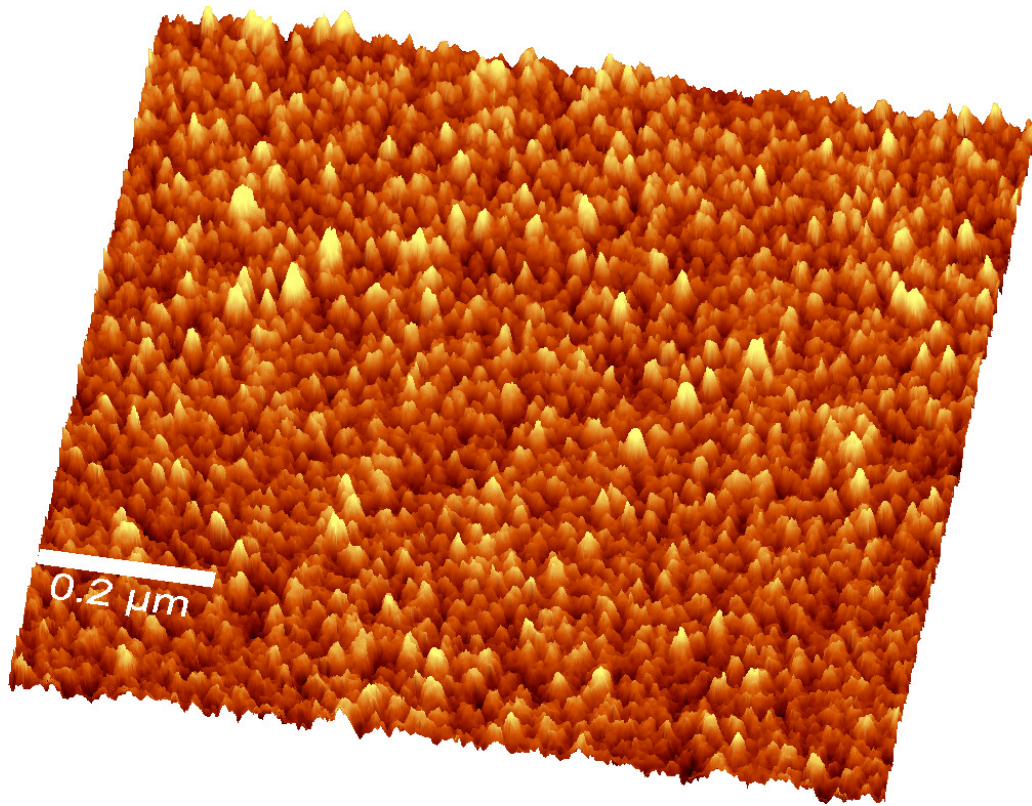


Figure 3.8: (a) AFM image of Ti (5%) doped WO₃ grown at a substrate temperature of 200 °C.

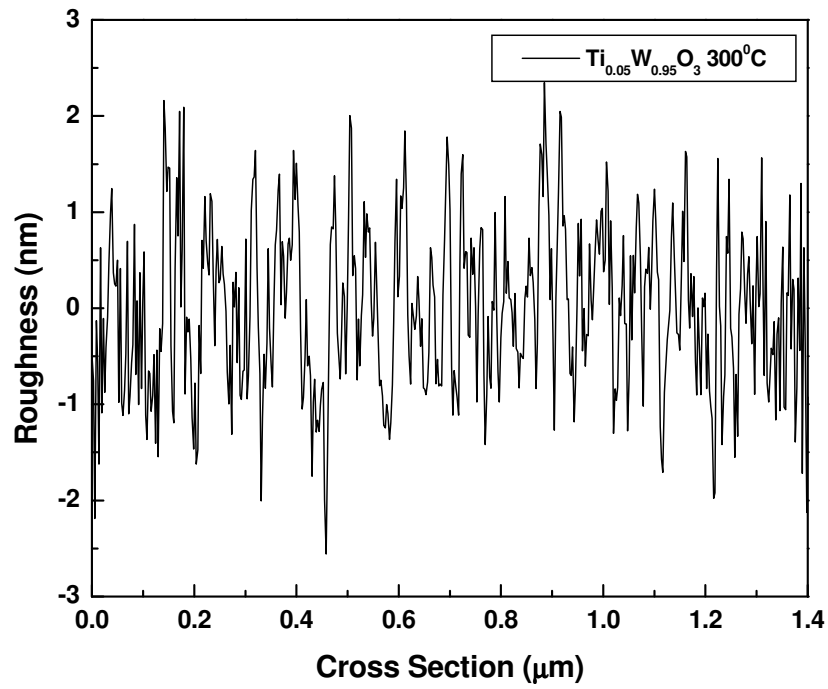
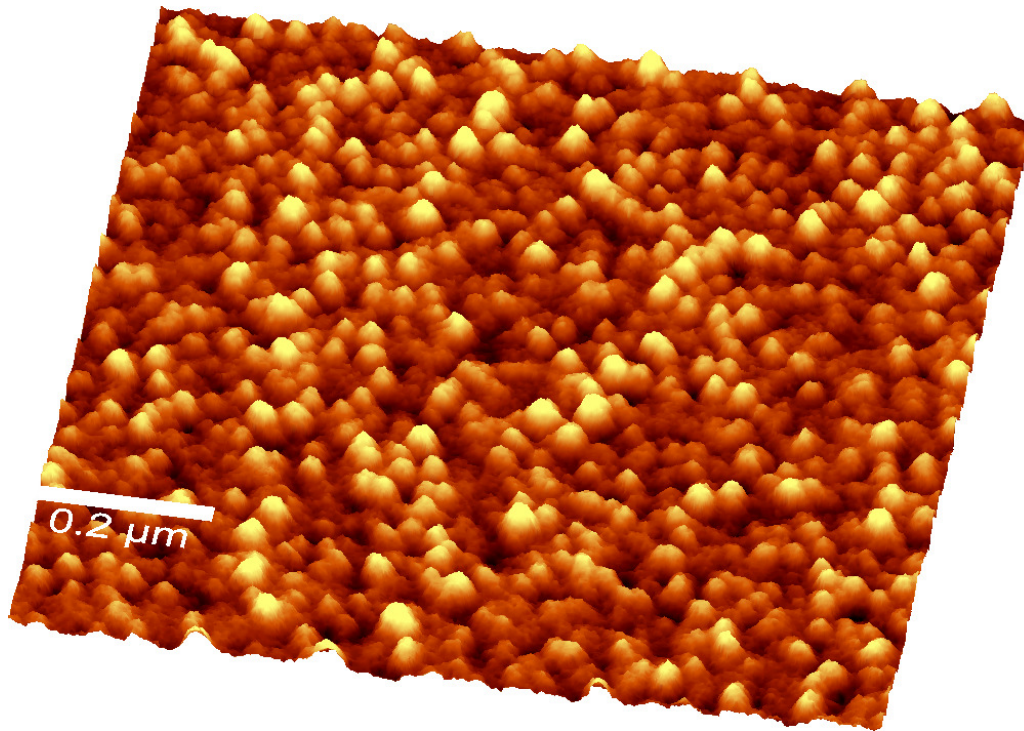


Figure 3.9: (a) AFM image of Ti (5%) doped WO₃ grown at a substrate temperature of 300 °C.

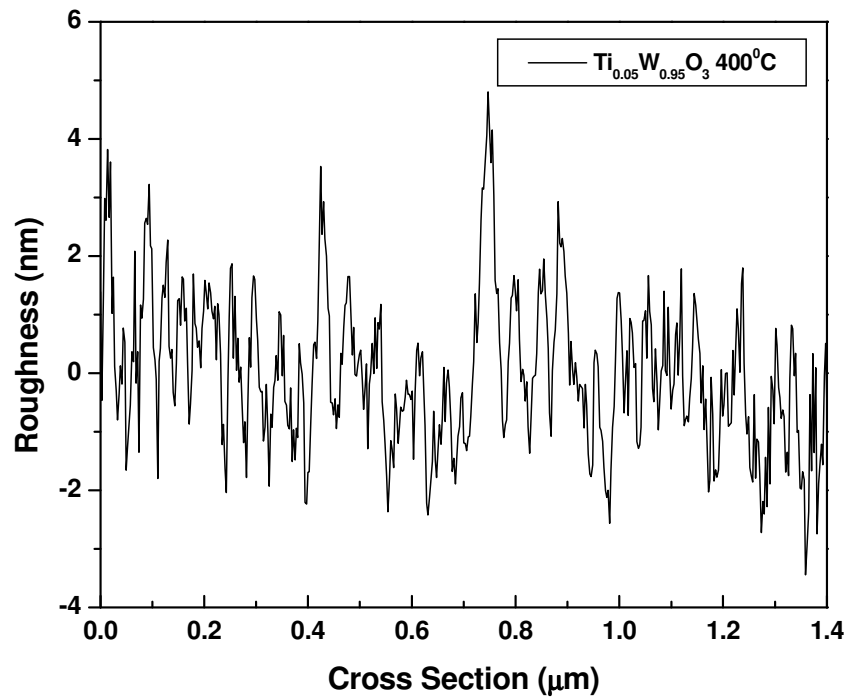
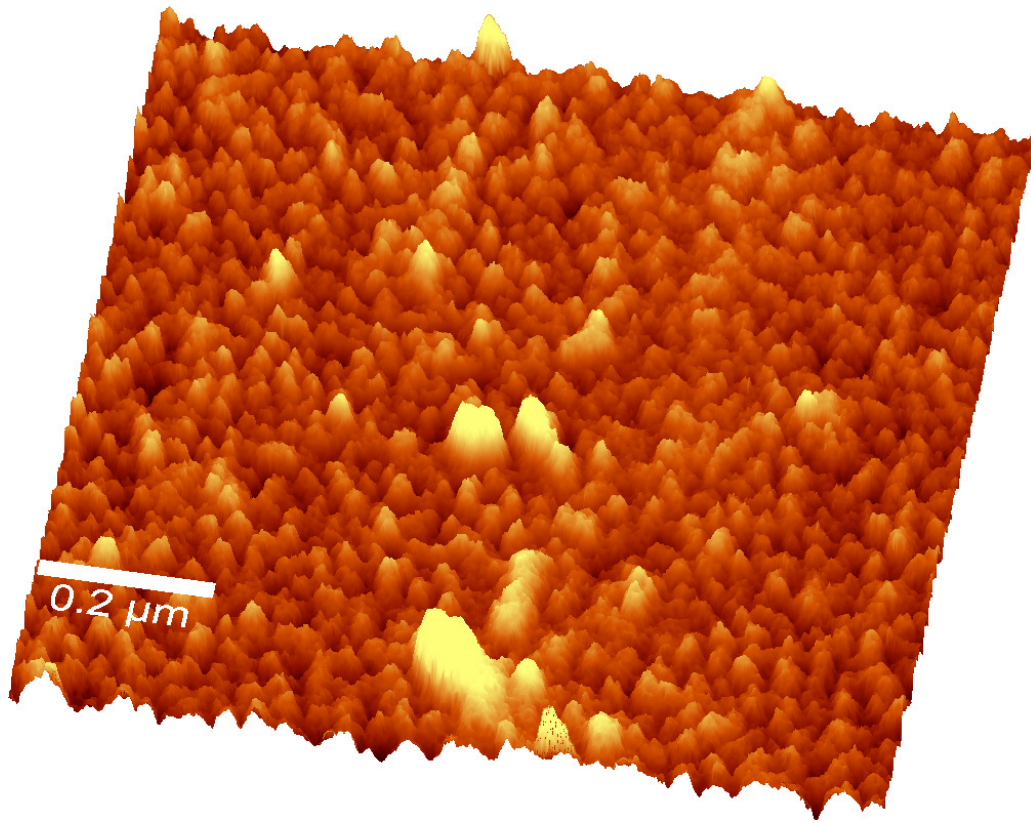


Figure 3.10: (a) AFM image of Ti (5%) doped WO₃ grown at a substrate temperature of 400 °C.

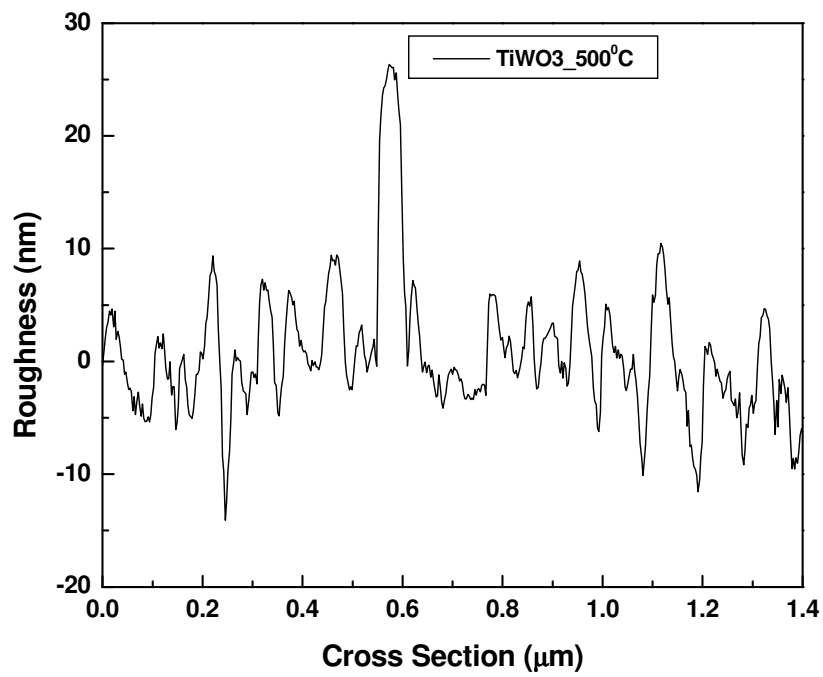
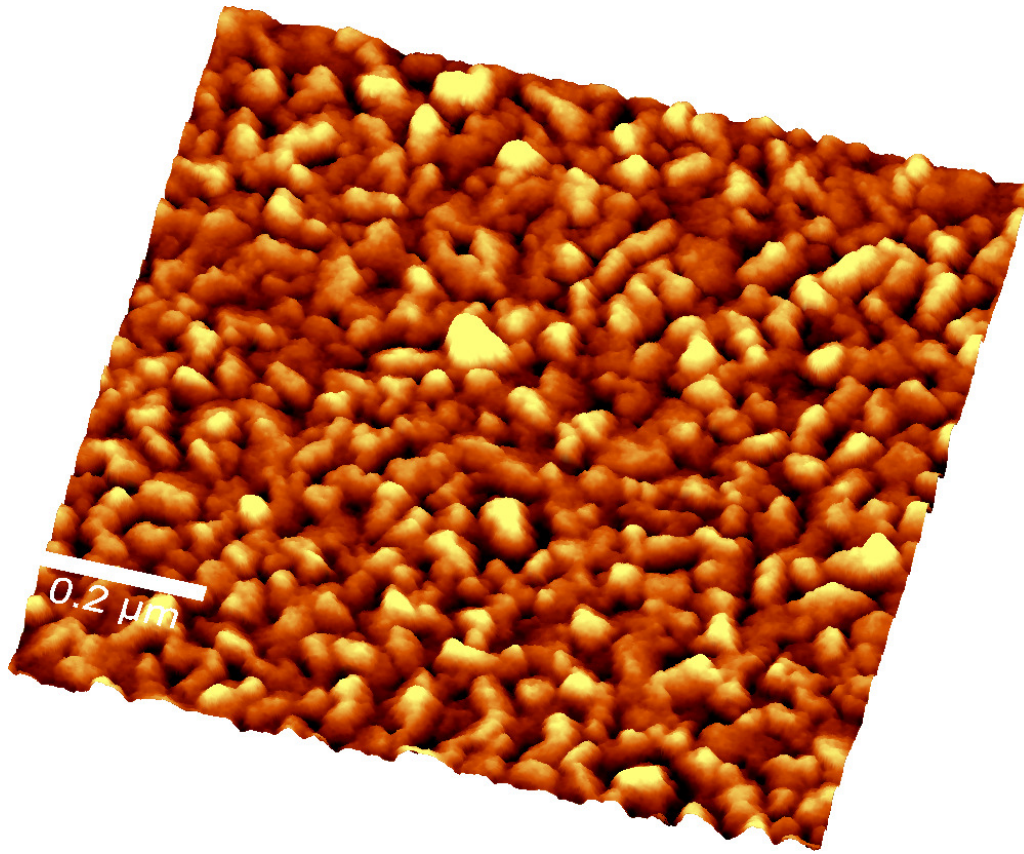


Figure 3.11: (a) AFM image of Ti (5%) doped WO_3 grown at a substrate temperature of 500 °C.

Very similar trend that was observed in pure WO_3 also revealed to the Ti (5%) doped samples, as seen from Figures 3.7 – 3.11 (b). If for a growth temperature is less than 300°C , the doped WO_3 films have a roughness of 2 nm, indicative of amorphous samples. At a growth temperature of 500°C the roughness becomes 8 nm. Also, the grain size of 5% doped sample at 500°C is half of the size of pure WO_3 sample at 500°C . The graphical relationships between the average particle size (L) and the surface roughness as functions of growth temperature are shown in Figure 3.12 (a) and (b), respectively.

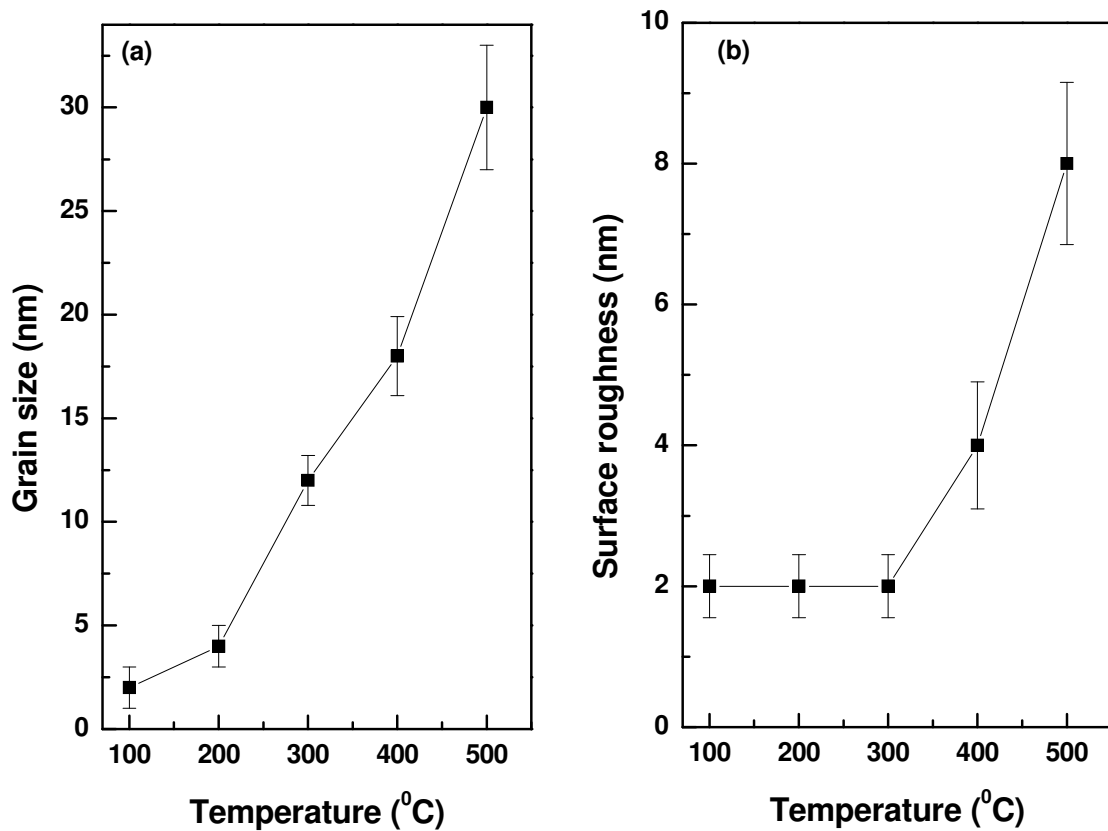


Figure 3.12: (a) Grain size and (b) surface roughness vs. temperature for Ti(5%) doped WO_3 films.

3.4 X-RAY DIFFRACTION RESULTS FOR WO₃ AND Ti(5%) DOPED WO₃ THIN FILMS

The XRD patterns for the pure WO₃ samples grown at different substrate temperatures, as labeled, are presented in Figure 3.12. They are vertically translated for clarity. Since the XRD spectrum of the film grown at room temperature did not show any peaks, we do not include it in Figure 3.12. The (002) XRD peak corresponding to the WO₃ phase appears when the temperature is 100 °C. However, this peak (at 23.19°) is rather broad, indicating very small particles, as previously observed in AFM measurements.

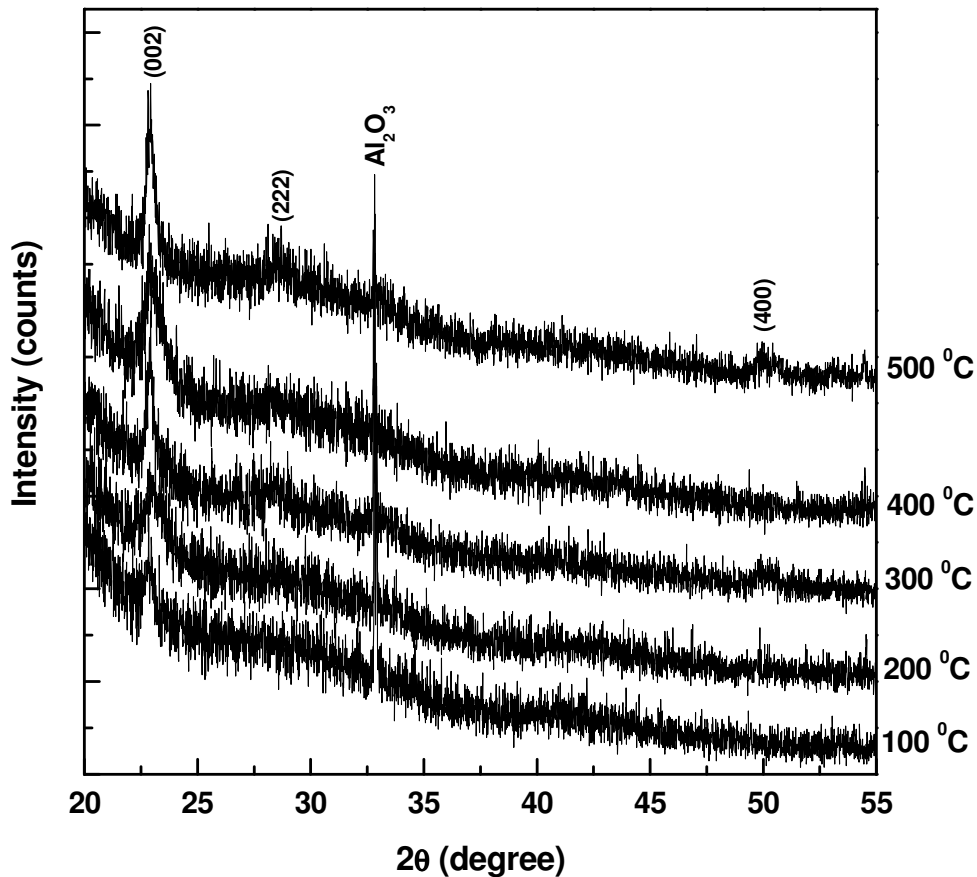


Figure 3.13: X-ray diffraction patterns of WO₃ films as a function of temperature.

It is evident from Figure 3.12 that the intensity of the peak at 23.19° , corresponding to diffraction from (002) planes of WO_3 , increases with increasing temperature, indicating an increase in the average crystallite-size with increasing temperature. This observation is again in good agreement with the above AFM results. However, comparison of our results with standard XRD diffraction spectra of monoclinic WO_3 , [63,64] which, in this diffraction region, should exhibit three strong characteristics peaks at $2\theta = 23.19^\circ$, 23.65° , and 24.37° corresponding to (002), (020), and (200) planes, respectively, show no presence of the latter two diffraction peaks. This highlights that the growth of the thin films is preferentially (002) oriented. This preferred orientation along (002) is dominant for WO_3 films grown at temperatures $\geq 200^\circ\text{C}$, and can be attributed to an increasing degree of preferred orientation with increasing temperature. Anisotropy exists in crystalline materials and the strain energy densities will typically be different for different crystallographic directions and the growth will favor those orientations with low strain energy density. The preferred (002) orientation of WO_3 films, therefore, can be explained based on the growth process minimizing the internal strain-energy in the film. Thus, an increase in temperature favors the preferred orientation along (002) while minimizing the strain-energy in the WO_3 film on the Si(100) surface.

The XRD patterns of Ti (5%) doped WO_3 films are shown in Figure 3.13. A background subtraction was performed for the XRD spectra. The XRD patterns of the samples grown at temperatures between RT and 200°C did not show any peaks, indicating their characteristic amorphous nature. Relevant diffraction peaks begin to appear in XRD patterns when substrate growth temperature is 300°C , indicating film crystallization at this temperature. This result corroborates the AFM experimental results, presented above.

Also, the crystallization temperature noted for Ti-doped WO_3 films is higher than that of pure WO_3 films. The effect of Ti is remarkable in preventing crystallization of WO_3 and raises its crystallization temperature. The XRD peak at 22.4° is rather broad, indicating the presence of

nanocrystallites. The integrated intensity of this peak, which corresponds to diffraction from (002) planes, increases with increasing substrate temperature. This is indicative of an increase in the average crystallite-size and preferred orientation of the film along (002) with substrate temperature increasing. This behavior is quite similar to that observed in pure WO_3 films.

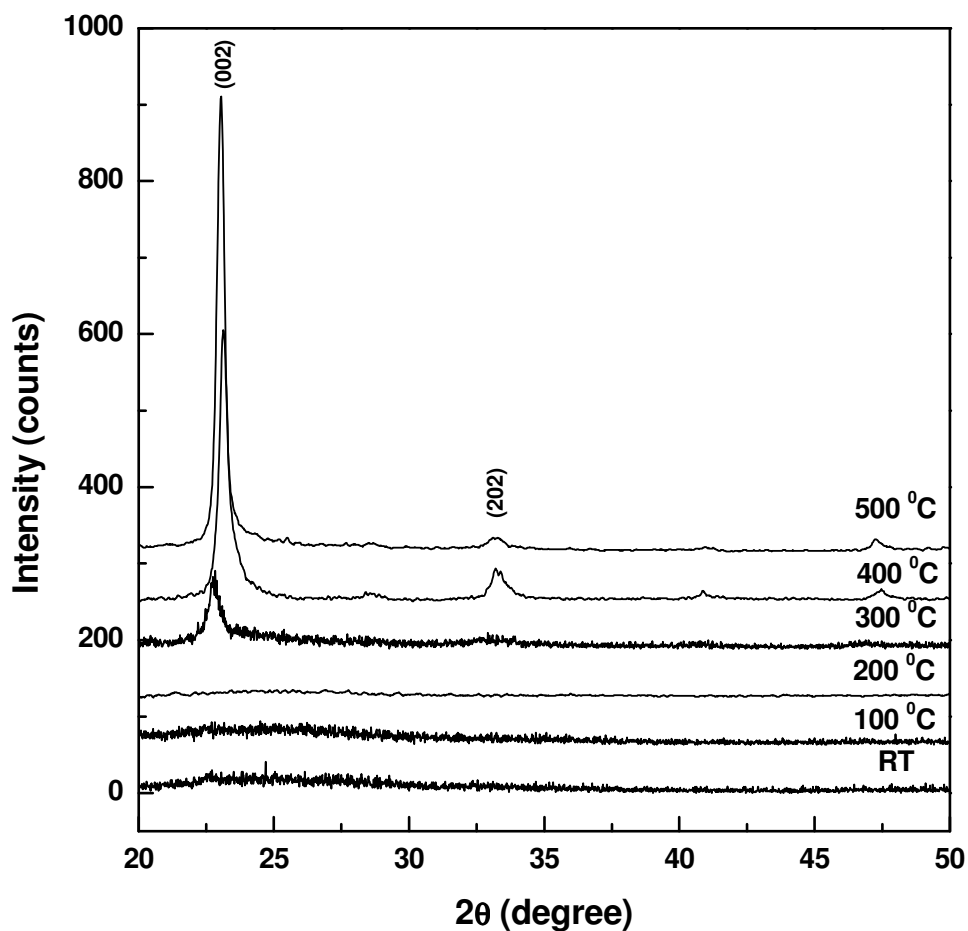


Figure 3.14: X-ray diffraction patterns of Ti(5%) doped WO_3 films as a function of temperature.

Again, the preferred c -axis orientation of $\text{W}_{0.95}\text{Ti}_{0.05}\text{O}_3$ films could be due to the growth process minimizing the internal strain-energy in the film. Furthermore, no TiO_2 diffraction peaks were observed in the doped films, even at high growth temperatures.

The peak at 23.19° is shifted to a slightly higher 2θ angle in the Ti doped film, indicating a slight contraction of the unit cell and suggesting substitution of Ti for W in the crystal lattice. For easier visualization of this shift, we present in Figure 3.14 the two diffraction patterns of WO_3 and $\text{Ti}_{0.05}\text{W}_{0.95}\text{O}_3$ samples grown at a substrate temperature of 500°C .

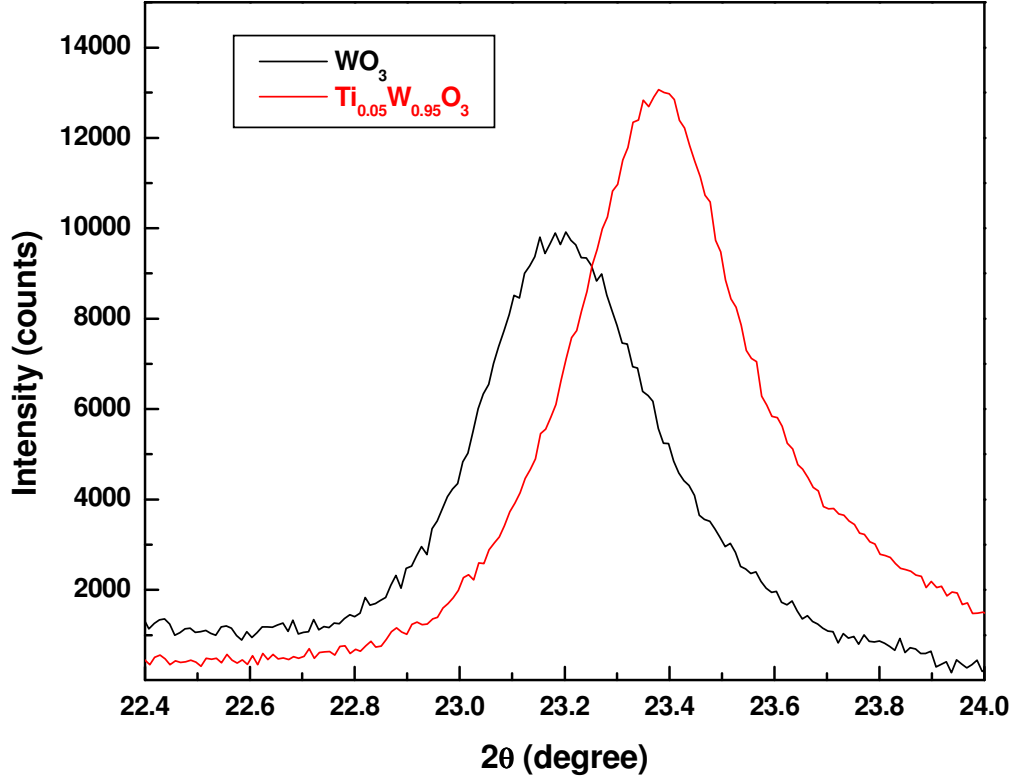


Figure 3.15: Comparison of the diffraction peaks around 23° 2θ angle of WO_3 and Ti(5%) doped WO_3 films grown at a substrate temperature of 500°C .

It is worth mentioning that Depero et al. [65] demonstrated that this cubic-like X-ray diffraction pattern might result from a static disorder introduced by edge-sharing octahedra randomly distributed in the lattice due to oxygen deficiency; thus, implying a lower stoichiometry of the doped samples as compared to that of undoped ones.

3.5 COMPARATIVE SPECTROSCOPIC RAMAN RESULTS FOR WO₃, Ti(5%) DOPED WO₃, AND Ti(20%) DOPED WO₃ THIN FILMS

To understand from a spectroscopic perspective how the growth temperature influences the crystallinity of the sample we first present the Raman results obtained in analyzing the pure WO₃ thin films.

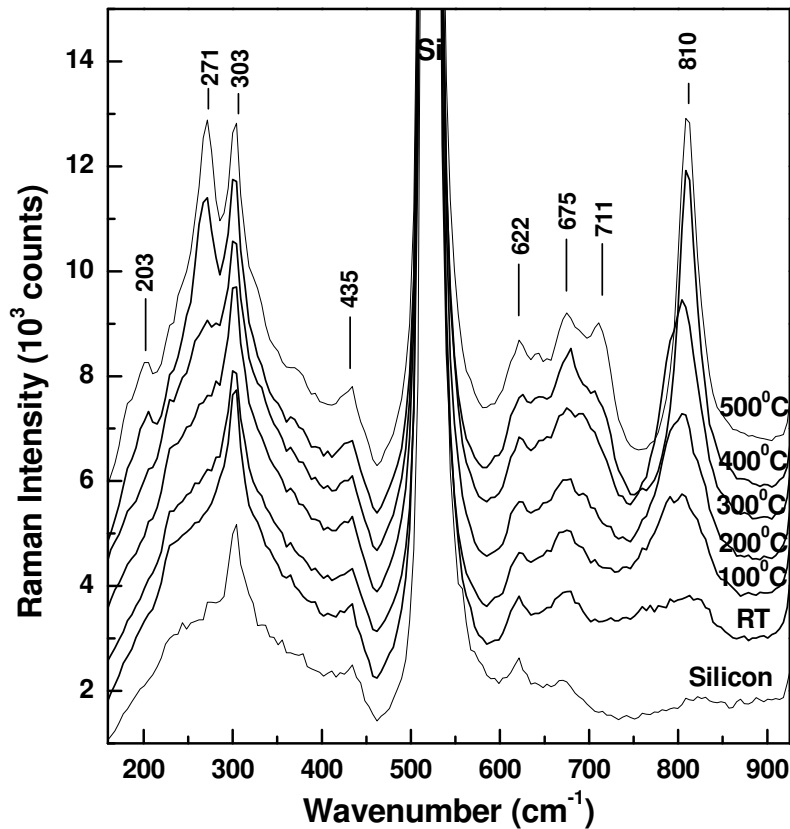


Figure 3.16: Raman spectra of WO₃ samples for varying Si substrate growth temperature.

These results, which are presented in Figure 3.14, have already been described in detail elsewhere.[66,67] They show an increase in the intensities of the vibrational lines around 271, 711, and 810 cm⁻¹ with increasing Si substrate temperature. Since these bands are characteristic of the Raman

spectra of monoclinic WO_3 , this is direct evidence of continuing crystallization of the material at higher temperatures, in agreement with AFM and XRD results discussed above.

Also, the Raman spectrum of the pure Silicon substrate is presented in this figure for easier comparison and for assignment of the features at 303, 435, 622, and 675 cm^{-1} to the unwanted but conspicuous presence of Si-O bonds. It is very well known that an Si wafer will always be covered by a very thin SiO_2 layer due to the high Si oxidation rate.

While the spectrum of the RT WO_3 sample is very similar to the Si spectrum, suggesting an amorphous WO_3 sample, a slight and an obvious increase in the intensities of the Raman peaks at 675 and 810 cm^{-1} , respectively, are observed for the samples grown at temperatures $\geq 100\text{ }^\circ\text{C}$, becoming more evident at higher temperatures. This observation confirms the beginning of material crystallization. Furthermore, for temperatures $\geq 300\text{ }^\circ\text{C}$, weak shoulders around 271 and 711 cm^{-1} can be observed in the spectra. These features transform into definite Raman peaks for temperatures of 400 and $500\text{ }^\circ\text{C}$. Since these vibrations, which are attributed to O-W-O modes of the bridging oxygens, were previously measured and reported in the literature for the monoclinic WO_3 structure, we assign this morphology to our thin films.

A look back in what is reported in the literature for the morphology of pure WO_3 as a function of growth temperature leads to Table 4.1, which is presented below. From this table, a structural transition from monoclinic to orthorhombic is expected at higher growth temperature. However, for 400 and $500\text{ }^\circ\text{C}$, the existence of a strained monoclinic morphology is observed instead.[66,67] Unfortunately, we could not perform Raman measurements at frequencies lower than 150 cm^{-1} , a region where a definite distinction between the two WO_3 structures can be achieved, due to the laser filter cutoff. However, to qualitatively identify the occurrence of monoclinic versus other strained WO_3 structures in the samples grown at high temperatures, confocal Raman mapping was performed and the results were explained and presented elsewhere.[66,67]

Table 4.1: Literature reported WO₃ structural phases as function of temperature.[68]

Temperature	WO ₃ structure
-25 to 20-30 °C	triclinic
20-30 to 330 °C	monoclinic
330 to 740 °C	orthorhombic
740 to 1473 °C	tetragonal

Since the current work is focusing on understanding how doping with Ti influences the morphology of the samples, in order to confirm morphological changes that might arise, we first present in what follows the Raman results when a high Ti concentration, of 20%, is used. This investigation will be followed by a comparison between undoped and doped samples where both percentages of doping, namely 5% and 20% are considered.

Again, for the samples doped with 20% Ti, we consider the growth at different substrate temperatures, which range from RT to 500 °C, in increments of 100 °C. The Raman results of this investigation are presented in Figure 3.15. As can be observed from these data, all the Raman spectra exhibit similar features such as the peaks at 303, 435, 622, and 672 cm⁻¹, which are associated with Si-O bonds, and a very weak and broad band at 810 cm⁻¹ that can be attributed to WO₃.

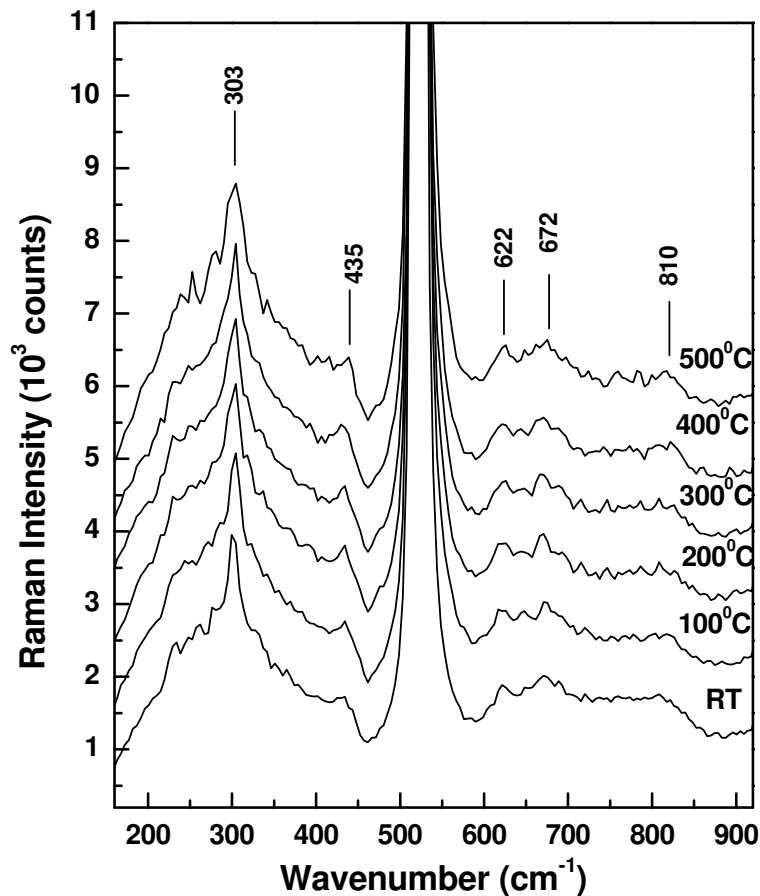


Figure 3.17: Raman spectra of Ti(20%)-doped WO_3 samples grown at Si substrate temperatures ranging between RT and 500 $^{\circ}\text{C}$.

Therefore, from these Raman results we might consider two possibilities: (1) the growth of crystalline samples with very small sizes even at room temperature, or (2) the scenario that all the samples are amorphous and the variation of substrate growth temperature had no effect. Due to the weakness and broadness of these bands, together with the fact that most of them belong to Si-O bonds, the latter scenario is more plausible.

As mentioned above, for comparison and for reassuring that the Ti(20%)-doped WO_3 samples have an amorphous nature we present in Figure 3.16 the Raman spectra of pure, Ti(5%)-doped, and Ti(20%)-doped WO_3 samples grown at a substrate temperature of 500°C .

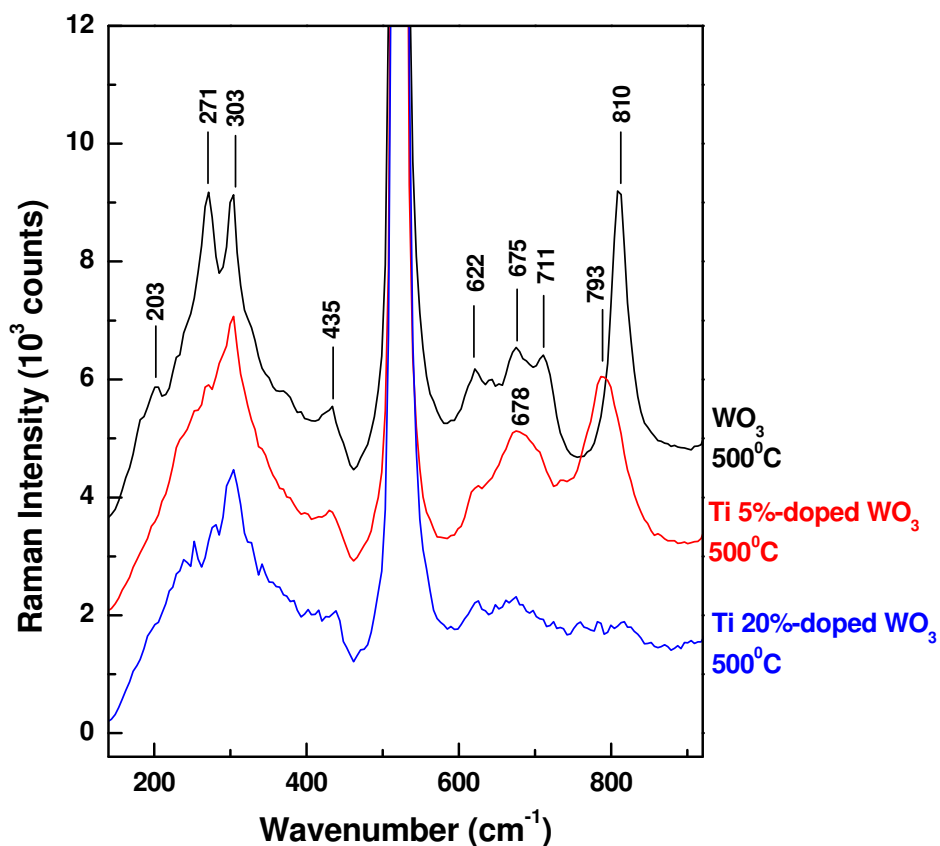


Figure 3.18: Raman spectra of pure, Ti(5%)-, and Ti (20%)-doped WO_3 samples grown at a substrate temperature of 500°C .

As is evident from these spectra, while the WO_3 material is crystalline with strong, definite vibrations, especially the one at 810 cm^{-1} which is attributed to W-O bonds, the other samples reveal only broad and weak bands in the same spectral region. Thus, definitely, the Ti(20%)-doped WO_3 sample has an amorphous nature. Also, a comparison between the spectrum of pure WO_3 and that of

Ti(5%)-doped WO_3 demonstrates that doping with a low concentration of Ti contributes to a change in material crystallization, an affirmation supported by the previous XRD data. However, from the Raman perspective, this remark is based on the observed shifting to lower frequencies of the Raman peaks corresponding to W-O-W stretching modes of WO_3 at 810 and 711 cm^{-1} , to 793 and 678 cm^{-1} , respectively. Also, higher growth temperatures are required to obtain crystalline microstructure for Ti(5%)-doped WO_3 films than for WO_3 films.

3.6 INFRARED ABSORPTION RESULTS FOR Ti(20%) DOPED WO_3 THIN FILMS

More evidence of the amorphous nature of the Ti(20%) doped WO_3 samples come from the infrared absorption data presented in Figure 3.17.

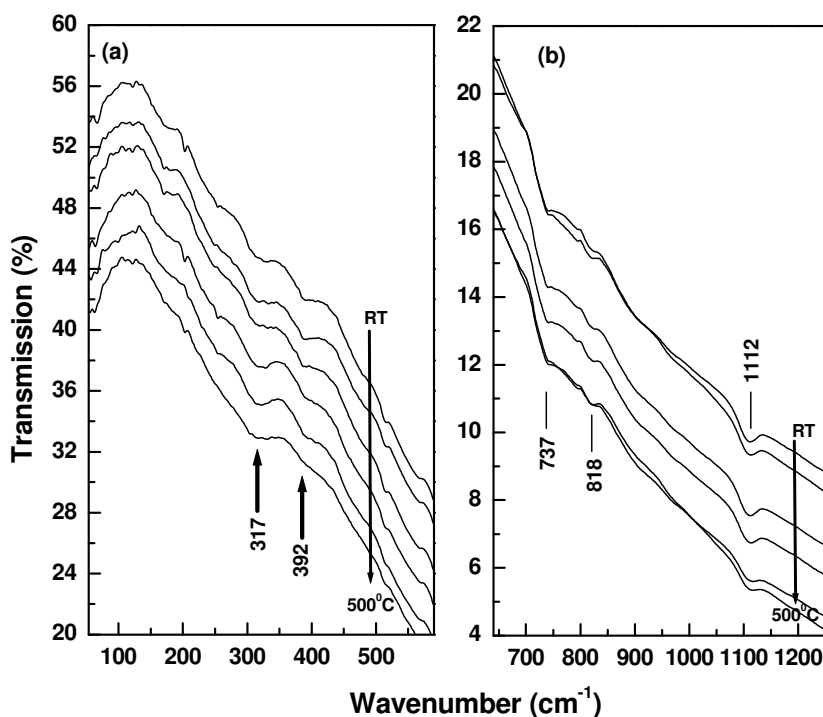


Figure 3.19: Infrared absorption spectra of Ti(20%)-doped WO_3 samples grown at

Si substrate temperatures ranging between RT and 500 $^{\circ}\text{C}$.

3.7 RAMAN AND INFRARED ABSORPTION RESULTS FOR Ti(5%) DOPED WO₃ THIN FILMS ANEAELED AT 600 °C AND 900 °C

Next, to see if there were any microstructure changes we performed Raman scattering and infrared absorption spectroscopy analyses on Ti(20%) doped WO₃ samples annealed in an open furnace. The samples were annealed at 600 °C and 900 °C. The outcomes of these spectroscopic investigations are presented in Figures 3.18 and 3.19 below.

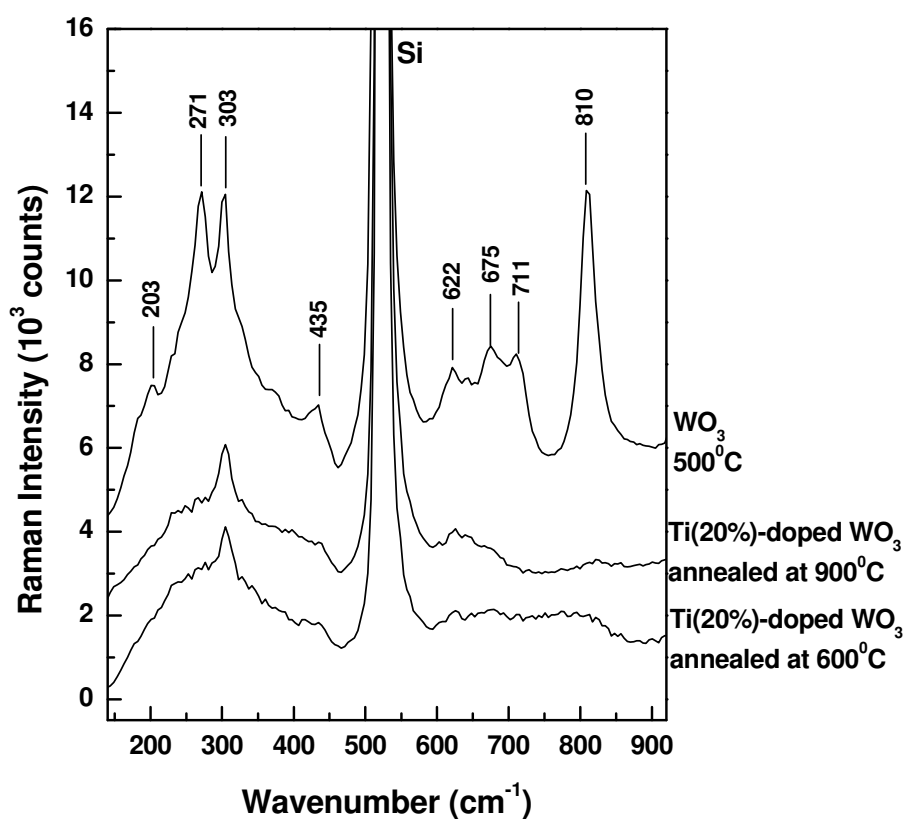


Figure 3.20: Raman spectra of Ti(20%)-doped WO₃ samples annealed at 600 °C and 900 °C.

For comparison, the spectrum of pure WO₃ grown at a substrate temperature of 500 °C is presented, too.

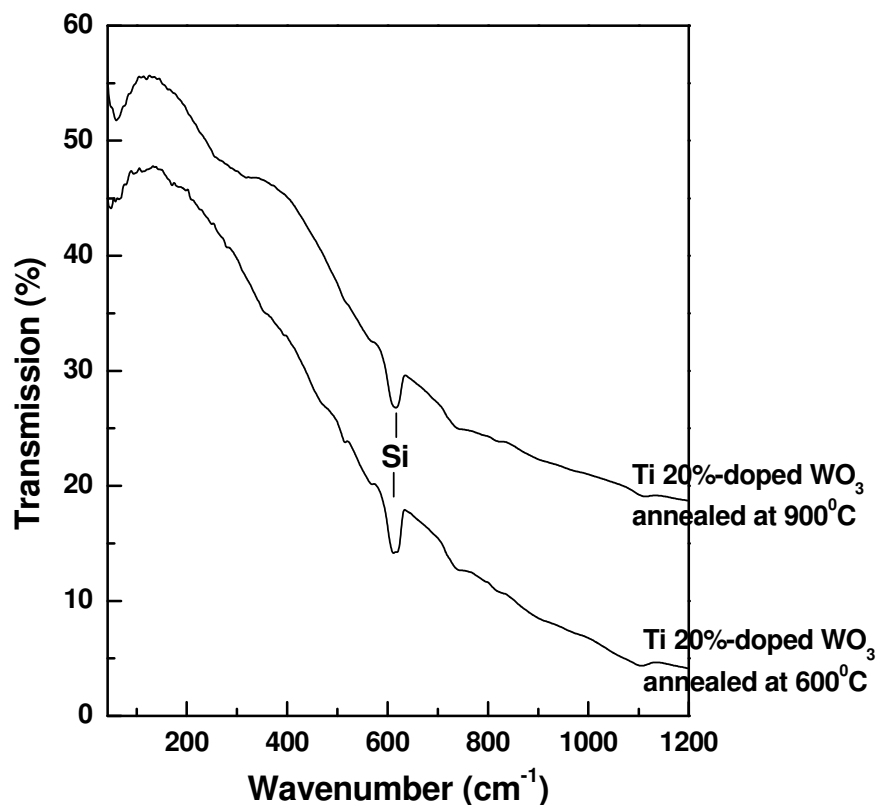


Figure 3.21: Infrared absorption spectra of Ti(20%)-doped WO_3 samples annealed at 600 $^{\circ}\text{C}$ and 900 $^{\circ}\text{C}$.

Again, for comparison we present in Figure 3.18 the spectrum of pure WO_3 grown at a substrate temperature of 500 $^{\circ}\text{C}$. As was evident from the Raman spectrum of this sample, the WO_3 material is crystalline; there are strong, definite vibrations in this spectrum, especially the one at 810 cm^{-1} which is attributed to W-O bonds. On the other hand, the sample annealed at 600 $^{\circ}\text{C}$ revealed only broad and weak bands in the same spectral region. Thus, even when annealed, the Ti(20%)-doped WO_3 sample exhibits an amorphous nature. Also, a comparison between the spectrum of pure WO_3 and that of Ti(20%)-doped WO_3 annealed at 900 $^{\circ}\text{C}$ demonstrates that annealing processes didn't contribute substantially to crystallization. However, there is a small increase in the intensity of the band at 635 cm^{-1} .

¹, an increase that indicates a possible segregation of the TiO₂ phase at this high annealing temperature. The infrared absorption data presented in Figure 3.19 corroborate with these findings, revealing mainly an amorphous nature for the annealed samples.

These studies confirm that the Ti 20% incorporation induces a significant disorder, which cannot be eliminated even upon external annealing.

Chapter 4: Conclusion and future work

4.1 CONCLUSION

As revealed in this study, the characteristics of pure WO_3 , a known candidate for being a good material for different industrial types of applications such as electrochromic camera displays, anti-dazzling rear view mirrors for automobiles, smart windows and glass facades that can regulate visible light and solar energy, catalytic/photocatalytic, humidity, temperature, gas, and bio-sensing devices, are strongly dependent on the conditions and methods used in its production. Thus, detailed information about the structural and spectroscopic properties of pure WO_3 is essential before advancing to analysis of other tungsten oxide types of engineered materials (e.g. morphological modification induced by doping).

Having established conditions for achieving improved quality (e.g., sensitivity, selectivity, and stability) of undoped thin films of WO_3 , the current work is based on the investigation of the effects of doping the WO_3 with different amounts of Ti (e.g. 5% and 20%), with the objectives of improving the quality of material and expanding its operating temperature ranges, especially at high temperatures. In this context, whereas WO_3 and Ti in pure forms have been investigated intensively in the literature, not many studies have been done for Ti doped WO_3 .

Also, an important question to consider is the degree to which doping can affect the porosity of the WO_3 film structure and/or its chemistry, which can have an influence on the number of surface active sites, which ultimately determine the effective surface area of the material, and, consequently, is connected with its sensitivity. Thus, the outcomes of the microscopic, structural, and spectroscopic comparative studies, which are summarized in what follows, will bring valuable insights for the potential applicability of this new designed material.

With increasing growth temperature, the AFM results for WO₃ films show increases in the average crystallite size from 10-14 nm at RT to more than 60 nm at 500 °C, and in the surface roughness from 4 nm at RT to about 8 nm at 500 °C.

The AFM data, along with the XRD and Raman results clearly indicate that for the given set of experimental conditions, a temperature slightly higher than 200 °C is necessary for promoting the growth of nanocrystalline WO₃ films with almost spherical particles. The amorphous WO₃ sample grown at RT starts crystallizing into a monoclinic WO₃ structure for temperatures between 100 and 300 °C. For 400 and 500 °C, the existence of a strained WO₃ structure is observed together with the monoclinic one in the Raman spectra.

Comparison of the AFM topography images for W_{0.95}Ti_{0.05}O₃ samples, which were grown using temperature conditions identical to those applied to the WO₃ thin films, shows that a higher temperature of at least 300 °C is required to obtain crystalline microstructure for Ti(5%)-doped WO₃ films than for WO₃ films. Also, for crystalline samples, a smaller average size of Ti-doped WO₃ nanoparticles is obtained, at the same high temperatures, than for undoped WO₃ materials, *e.g.*, at a substrate temperature of 500 °C the average size observed in the image of the W_{0.95}Ti_{0.05}O₃ sample is ~30 nm as compared to the value of ~60 nm seen for the AFM image of the undoped sample.

These remarks are further supported by the XRD data, where, in addition, a slight shift of the peak at 23.19° corresponding to (002) planes of monoclinic structure, to slightly higher 2θ angle in the Ti doped film is observed. This shift is an indication of a slight contraction of the unit cell, suggesting also a disorder effect introduced by doping, with substitution of Ti for W in the crystal lattice.

Similar morphological changes induced by the 5% Ti doping were revealed by Raman measurements, where shifting to lower frequencies of the Raman peaks corresponding to W-O-W stretching modes of WO₃ at 810 and 711 cm⁻¹, to 793 and 678 cm⁻¹, respectively, were observed.

Comparison of these data with the ones reported in the literature suggests a possible change of monoclinic structure to an orthorhombic configuration, but more probably a tetragonal one.

Having understood the science and phenomena associated with Ti-doped WO_3 with a small amount of Ti (5%), we initiate the work on doping Ti at a higher level of concentration. The Raman results demonstrate that Ti 20% incorporation induces a significant disorder into the tungsten oxide material, with the outcome of a completely amorphous nature for the samples. These observations are confirmed by infrared absorption measurements, too.

Finally, to see if there were any microstructure changes we performed Raman scattering and infrared absorption spectroscopy analyses on amorphous Ti(20%) doped WO_3 samples annealed in an open furnace at temperatures of 600 °C and 900 °C. Even when annealed at 600°C, the Ti(20%)-doped WO_3 sample exhibits an amorphous nature. For the sample annealed at 900 °C, a small increase in the intensity of the band at 635 cm^{-1} , which indicates a possible segregation of the TiO_2 phase, was observed. Thus, the annealing processes didn't contribute substantially to crystallization and improvement of material quality, demonstrating that Ti 20% incorporation induces a significant disorder, which cannot be eliminated even upon external annealing.

4.2 FUTURE WORK

As seen above, the concentration of the dopant is important in changing the morphology of WO_3 . Understanding the electronic structural changes associated with stabilization is fundamental to describing the structure-property relationships of a material. Therefore, computational analysis, where incrementally increasing amounts of Ti should be introduced to validate the proper Ti doping that will maximize material structural stability. Different programs such as Cerius (Accelrys Inc.), Gaussian, and other QM/MM software are already available for these types of calculations.

References

- [1] Minchener, A. J., Coal Gasification for Advanced Power Generation (2005).
- [2] K. Huang, Q. Zhang, F. Yang, D. He, *Nano-Res*, vol. 3, 281-287 (2010).
- [3] A. Hooker, Nanotechnology Advantages Applied to Gas Sensor Development, Nanoparticles Conference Proceeding (2002).
- [4] W. Callister, D. Rethwisch, Materials Science and Engineering: An Introduction, Wiley, 8 Editions, (2009).
- [5] H. Kawasaki, T. Matsunaga, W. Guan, *J. Plasma Fusion Res. Series*, vol. 8, 1431-1434 (2009).
- [6] C.G Granqvist., Handbook of Inorganic Electrochromic Materials, Elsevier, Amsterdam (1995).
- [7] S. Bechinger, S. Herminghaus, P. Leiderer, *Thin Solid Films*, vol. 239, 156-160 (1994).
- [8] K. Aguir, C. Lemire, D.B.B. Lollman, *Sensors and Actuators B*, vol. 84, 1-5 (2002).
- [9] A. Enesca, L. Andronic, A. Duta, S. Manolache, *Romanian Journal of Information Science and Technology*, Vol. 10, 269-277 (2007).
- [10] R.S. Khadayate, S.K. Disawal, P.P. Patil, *Sensors & Transducers*, IFSA ISSN, 1726-5479, (2009).
- [11] K. Galatsis, Y.X. Li, W. Wlodarski, E. Comini, G. Sberveglieri, C. Cantalini, S. Santucci, M. Passacantando, *Sensors and Actuators B*, vol. 83, 276-280 (2002).
- [12] W. Gopel, K. Schierbaum, *Sensors*, Volume 2: Chemical and Biochemical Sensors, Winheim, p.2 (1991).
- [13] J. Stetter, W. Penrose, Understanding Chemical Sensors and Chemical Sensors Arrays (Electronic Noses): Past, Present, and Future, *Sensors Update*, vol. 2, 189-229 (2002).
- [14] J. Janata, *Principles of chemical sensors*, New York and London, Plenum Press (1989).
- [15] M. Madou, S. Morrison, *Chemical sensing with solid state devices*, San Diego, Academic Press (1989).

- [16] P. Molesey, B. Tofield, *Solid state gas sensors*, Bristol, Adam Hilger (1989).
- [17] P. Moseley, J. Norris, D. Williams, *Techniques and mechanisms in gas sensing*, Bristol, Adam Hilger (1991).
- [18] W. Gopel, W. Reinhardt, Metal Oxide Sensors: New Devices through Tailoring *Interfaces on the Atomic Scale*, Sensors Update, Vol. 1, 49-120 (1996).
- [19] W. Gopel, *Surf. Sci.*, vol. 62, 165-182 (1997).
- [20] S. C. Chang, *J. Vac. Sci. Technol.*, vol. 17, 366-369 (1980).
- [21] N. Yamazoe, J. Fuchigami, M. Kishikawa, T. Seiyama, *Surf. Sci.*, vol. 86, 335-344 (1979).
- [22] D.K. Benson, C.E. Tracy, H. Lee, “Low Cost, Fiber-Optic Hydrogen Gas Detector Using Guided-Wave, Surface-Plasmon Resonance in Chemochromic Thin Films” National Renewable Energy Laboratory, US Department of Energy, Contract Number DE-AC36-83CH100393 Golden Colorado, USA, (1998).
- [23] T. Maekawa, J. Tamaki, N. Miura, N. Yamazoe, *Chem. Letters*, 632-642 (1992).
- [24] N. Yamazoe, J. Tamaki, N. Miura, *Mat. Sci. Eng. B*, Vol. 41, 178-181 (1996).
- [25] X. Wang, N. Miura, N. Yamazoe, *Sens. Actuators B*, Vol. 66, 74-76 (2000).
- [26] S. Biaggio, R. Rocha-Filho, *J. Brazil Chem. Soc.*, vol. 5 123-126, (1994).
- [27] M. Stankova, X. Vilanova, J. Calderer, I. Gracia, C. Cane, C. Correig, *J. Optoelectronics and Advance Materials*, vol. 7, No. 3, 1237-1242 (2005).
- [28] D. Smith, J. Vetelino, R. Falconer, E. Wittman, *Sens. Actuators B*, vol. 13-14, 264-268 (1993).
- [29] M. Antonik, J. Schneider, E. Wittman, K. Snow, J. Vetelino, R. Lad, *Thin Solid Films*, vol. 256, 247-252 (1995).
- [30] S. Moulzolf, S. Ding, R. Lad, *Sens. Actuators B*, vol. 77, 375-282 (2001).
- [31] G.S. Trivikrama Rao, D Tarakarama Rao, *Gas sensitivity of ZnO based thick film sensor to NH₃ at room temperature*, Sensors and Actuators B: Chemical, vol. 55, 166-169 (1999).

- [32] Mei Chen, Zhihua Wang, Dongmei Han, Fubo Gu,* and Guangsheng Guo, *Porous ZnO Polygonal Nanoflakes: Synthesis, Use in High-Sensitivity NO₂ Gas Sensor, and Proposed Mechanism of Gas Sensing*, dx.doi.org/10.1021/jp201816d | J. Phys. Chem. C, 115, 12763–12773 (2011)
- [33] Zhang, N. Yu, Ke Li, Q. Zhu, Z. Q. Wan, Q. ,*Room-temperature high- sensitivity H₂S gas sensor based on dendritic ZnO nanostructures with macroscale in appearance*, Journal of Applied Physics, vol. 103, 104305 - 104305-6 (2008)
- [34] N. Basan, U. Weimar, Understanding the fundamental principles of metal oxide gas sensors; the example of CO sensing with SnO₂ sensors in the presence of humidity, J. Phys.: Condens. Matter, vol. 15 R813-839, (2003).
- [35] V. Smatko, V. Golovanov, Structural stability of In₂O₃ films as sensor materials, 2009, Springer Science+Business Media.
- [36] M. Ferroni, V. Guidi, G. Martinelli, *Characterization of a nanosized TiO₂ gas sensor*, Nanostructure Materials, vol. 7, 709-718 (1999)
- [37] NIOSH/OSHA: Occupational Health Guidelines for Chemical Hazards, National Institute for Occupational Safety and Health/Occupational Safety and Health Administration, January 1981.
- [38] D.N. Chavan, Nano Ag-doped In₂O₃ thick film: a low temperature H₂s gas sensor, (2009).
- [39] I. Simon, N. Barsan, M. Bauer, U. Weimar, *Sens. Actuators B*, vol. 73, 1-26 (2001).
- [40] Daintith, John (2005). *Facts on File Dictionary of Chemistry* (4th ed.). New York: Checkmark Books. ISBN 0816056498.
- [41] Lassner, Erik; Schubert, Wolf-Dieter (1999). "low temperature brittleness". *Tungsten: properties, chemistry, technology of the element, alloys, and chemical compounds*. Springer. p. 256. ISBN 9780306450532.

- [42] S. Tanisaki, Crystal structure of monoclinic tungsten trioxide at room temperature, Journal of the Physical Society of Japan, Vol. 15, No. 4, April 1960.
- [43] E. Salje, *The orthorhombic phase of WO₃*, Acta Cryst. B33, 574577, 1977
- [44] K.R. Locherer and K.H. Salje, *the refinement of a tetragonal phase of WO₃ using a novel PSD high temperature X-ray powder diffractometer*, Phase Transitions, vol. 69 85-83 (1999)
- [45] B. Pecquenard, Orthorhombic WO₃ Formed via a Ti-Stabilized WO₃ · 13H₂O Phase, Volume 135, Issue 1, Journal of Solid State Chemistry (2002).
- [46] M. Boulova and G. Lacazeau, *Crystallite Nanosize Effect on the Structural transitions of WO₃ Studied by raman Spectroscopy*, Journal of Solid State Chemistry, vol. 167, 425-434 (2002).
- [47] E. Cazzanelli, C. Vinegoni, G. Mariotto, A. Kuzmin, J. Purans, *Raman study of the phase transitions sequence in pure WO₃ at high temperature and in H_xWO₃ with variable hydrogen content*, Solid State Ionics, Volume 123, Issues 14, August 1999, Pages 6774, ISSN 01672738, DOI: 10.1016/S01672738(99)001010.
- [48] Y Shimizu and M. Egashira, *Basic aspects and challenges of semiconductors gas sensors*, MRS Bulletin (June 1999) 18-24.
- [49] D. D. Vuonga, G. Sakai^b, K. Shimano^b, N. Yamazoe, Hydrogen sulfide gas sensing properties of thin films derived from SnO₂ sols different in grain size, Sensors and Actuators B, vol. 105 (2005), 437-442.
- [50] J. Gong, Q. Chen, M. R. Lian, N.-C. Liu, R. G. Stevenson, Fatos Adami, Micromachined nanocrystalline silver doped SnO₂ H₂S sensor, Sensors and Actuators B, vol. 114 (2006), 32-39.
- [51] F.S. Manciu, J.L. Enriquez, W.G. Durrer, Y. Yun, C.V. Ramana, and S.K. Gullapalli: *"Spectroscopic analysis of tungsten oxide thin films"*, Journal of Materials Research, vol. 25, Issue 12, 2401-2406 (2010).

- [52] Franz, G., Advances in atomic force microscopy, *Reviews of Modern Physics* 75: 949,(2003)
- [53] Lapshin, R. V. ,Feature-oriented scanning methodology for probe microscopy and nanotechnology, *Nanotechnology* (UK: IOP) 15 (9): 1135–1151, (2004)
- [54] Eaton, P., *Atomic Force Microscopy*, 978-0-19-957045-4,Hardback, (2010)
- [55] Witec AFM Manuel, AFM AC Configuration, (2008)
- [56] <http://www.seas.upenn.edu/~chem101/sschem/solidstatechem.html>
- [57] http://en.wikipedia.org/wiki/X-ray_scattering_techniques
- [58] Kittel, C.; “Introduction to Solid State Physics.” *Wiley*, New York, (1968).
- [59] C. Suryanarayana, M. G. Norton, “X-ray Diffraction – a practical approach”, Plenum Press, (1998)
- [60] Ferraro, J., Nakamoto, K., Brown, C., “Introductory Raman Spectroscopy” American Press (2003).
- [61] http://en.wikipedia.org/wiki/Raman_spectroscopy
- [62] A. Hjelm, C.G. Granqvist, J.M. Wills, *Phys. Rev. B* 54 (1996) 2436.
- [63] Hong-tao Sun, carlo cantalini, Luca Lozzi, Maurizio Passacantando, Sandro Santucci, Mario Pelino, *Thin Solid Films* 287 (1996) 258-265.
- [64] C.V. Ramana, S. Utsunomiya, R.C. Ewing, C.M. Julien, U. Becker, *Phys. Stat. Sol. A*, vol. 202, No.10, 108-110 (2005).

- [65] L.E. depero, S. Groppelli, L.N. Sora, L. sangaletti, G. Sberveglieri, E. Tondello, J. Solid State Chem. 121 (1996) 379-387.
- [66] F.S. Manciu©, J.L. Enriquez, W.G. Durrer, Y. Yun, C.V. Ramana, and S.K. Gullapalli: “Spectroscopic analysis of tungsten oxide thin films”, Journal of Materials Research, vol. 25, Issue 12, 2401-2406 (2010).
- [67] Jose Luis Enriquez Carrejo M.S. thesis: “Spectroscopic analysis of tungsten oxide thin films for sensor applications”.
- [68] E. Cazzanelli, C. Vinegoni, G. Mariotto, A. Kuzmin, J. Purans, Raman study of the phase transitions sequence in pure WO₃ at high temperature and in H_xWO₃ with variable hydrogen content, Solid State Ionics, Volume 123, Issues 14, August 1999, Pages 6774, ISSN 01672738, DOI: 10.1016/S01672738(99)001010.

Vita

Young Yun

Material Science and Engineering

Young Yun earned his Bachelor of Engineering degree in Mechanical Engineering from the University of Texas at El Paso (UTEP) in 2002. He also received his Master of Science degree in Mechanical Engineering in 2004 from UTEP. After working as design engineer and serving our nation as reserve officer, he joined the doctoral program in 2009.

Dr. Yun has been the recipient of numerous honors and awards including University of Texas at El Paso Dodson Fellow Award and Cotton Memorial Scholarship. He was also supported by the United States Navy after serving in the operation of enduring freedom under the post 9/11 GI Bill and Hazlewood Act.

While pursuing his degree, Dr. Yun worked as Research Assistant and Teaching Assistant in the department of Physics in UTEP while keeping his duty as officer in charge for the El Paso Detachment.

Dr. Yun has presented his research at various conference meetings and workshops, including the 2011 Southwest Energy Science and Engineering Symposium, American Physical Society meeting, and Doctoral Research Exposition that was held at UTEP.

Dr. Yun's dissertation, entitled "Microscopic and Spectroscopic Analysis of WO₃ and Ti-doped WO₃ Thin Films," was supervised by Dr Felicia Manciu.

Permanent address: 1213 Franklin Nook
El Paso, TX, 79912

This dissertation was typed by Young T. Yun.